Coordination Chemistry Reviews 255 (2011) 774–789

Contents lists available at ScienceDirect

Coordination Chemistry Reviews

journal homepage: www.elsevier.com/locate/ccr

Review

Recent advances in understanding blue copper proteins

Edward I. Solomon*, Ryan G. Hadt

Department of Chemistry, Stanford University, Stanford, CA 94305, USA

Contents

ARTICLE INFO

Article history:
Received 12 October 2010
Received in revised form 6 December 2010
Accepted 7 December 2010
Available online 16 December 2010

Keywords:
Blue Cu
Axial ligand
Entatic state
Rack-induced state
Coupled distortion
Electron transfer
Spectroscopy
DFT calculation
TD-DFT calculation
Temperature dependence
Reduction potential
Thermodynamics

ABSTRACT

The type 1 (T1) or blue Cu (BC) proteins are a highly studied group of electron transfer (ET) active sites in bioinorganic chemistry. In this review, we cover several more recent results which extend the understanding of the geometric and electronic structure of these interesting Cu ET sites. Spectroscopic methods in tandem with density functional theory (DFT) and time dependent-DFT (TD-DFT) calculations have been used in studies of S → Se variants as well as a series of metal-varied model complexes ($M = Mn^{2+} \rightarrow Zn^{2+}$). The ligand and metal perturbations further defined the origins of the unique spectral features of BC proteins. These unique spectral features show different temperature dependencies in different T1 sites, and contrasts drawn between their behaviors define the role of the protein in tuning the geometric and electronic structure of the BC site for function. This has been termed the 'entatic' or 'rack-induced' state in bioinorganic chemistry.

Abbreviations: BC, blue Cu; LF, ligand field; T_d, tetrahedral; LMCT, ligand-to-metal charge transfer; Pc, plastocyanin; Az, azurin; Paz, pseudoazurin; CBP, cucumber basic protein; NiR, nitrite reductase; Am, amicyanin; MCO, multicopper oxidase; MO, molecular orbital; RAMO, redox active molecular orbital; ET, electron transfer; T1, type 1; DFT, density functional theory; TD-DFT, time dependent density functional theory; XPS, X-ray photoelectron spectroscopy; EPR, electron paramagnetic resonance; XAS, X-ray absorption spectroscopy; EXAFS, extended X-ray absorption fine structure; MCD, magnetic circular dichroism; rR, resonance Raman; LT, low temperature; RT, room temperature; SO, spin-orbit; WT, wild-type; PED, potential energy distribution; FWHM, full width at half maximum; L, hydrotris(3,5-diisopropyl-1-pyrazolyl)borate; pz, pyrazolyl.

* Corresponding author.
E-mail address: edward.solomon@stanford.edu (E.I. Solomon).

0010-8545/$ – see front matter © 2010 Elsevier B.V. All rights reserved.
doi:10.1016/j.ccr.2010.12.008

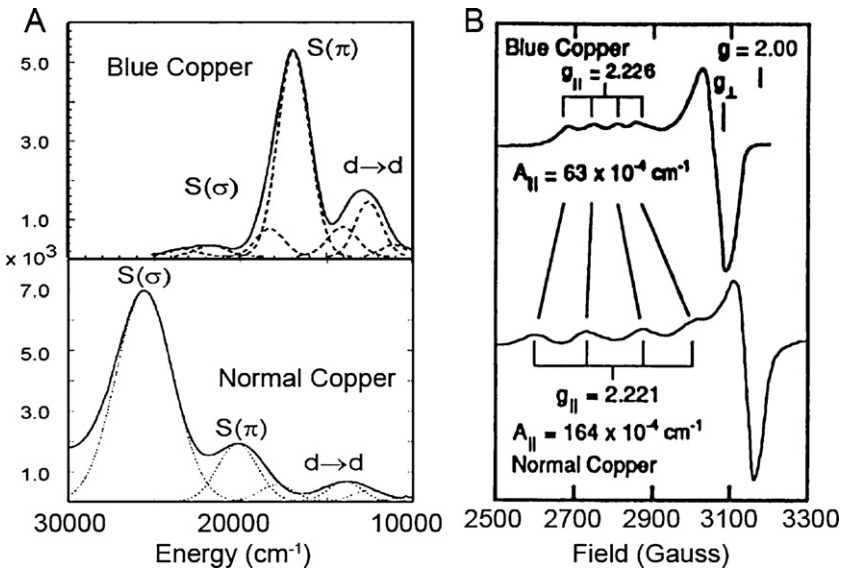

Fig. 1. (A) Comparison of blue Cu and normal Cu absorption spectra. (B) X-band EPR spectra of blue Cu (top) and normal Cu (bottom). (The normal Cu absorption spectrum is represented by nitrosocyanin where the large change in ligand field relative to plastocyanin described in Ref. [101] leads to a σ bonded thiolate to Cu^{2+}). Adapted from Ref. [100].

1. Introduction

The blue Cu (BC) or type 1 (T1) proteins [1] carry out electron transfer (ET) [2–5] in a wide variety of biological systems with variable enzymatic architectures. From the early days of bioinorganic chemistry researchers were fascinated by the unique spectral features of the BC proteins [1]. An intense absorption band ($\varepsilon \sim 5000\ M^{-1}\ cm^{-1}$) in the ~600 nm red spectral region gives them their bright blue color. They were an early focus of electron paramagnetic resonance (EPR) spectroscopy as they exhibited a very weak interaction of the unpaired electron spin with the nuclear moment of the Cu^{2+} ion. The presence of these unique spectral features led to the concept of an 'entatic' [6,7] (Vallee and Williams) or 'rack-induced' [8] (Malmström) state in bioinorganic chemistry; loosely the idea that the protein can impose an unusual geometric and electronic structure on the metal ion activating it for reactivity.

In 1976 Harry Gray, Jeff Hare, and I showed that the BC proteins exhibited low energy ligand field (LF) transitions indicating that they must have a pseudo-tetrahedral (T_d) structure [9], and from S_{2p} X-ray photoelectron spectroscopy (XPS) [10] these sites had a Cu–S(Cys) bond. These spectroscopic insights were confirmed by the first crystal structure of a BC protein, that of plastocyanin (Pc) by Freeman [11,12], which showed the BC center did indeed have a distorted T_d LF consisting of a strong equatorial S(Cys) (~2.1 Å), a weak axial S(Met) (~2.9 Å), and two N(His) ligands (~2.0 Å). The preferred coordination environment in most Cu^{2+} complexes is square planar due to the Jahn–Teller distorting force present in the cupric state. The distorted T_d active site in Pc would then be consistent with an 'entatic' or 'rack-induced' state, wherein the protein matrix imposes the reduced (Cu^+) geometry upon the oxidized (Cu^{2+}) site, activating it for rapid ET. Later in the review we show how this is not, in fact, the appropriate way to view the influence of the protein constraints in BC sites.

Normal tetragonal cupric complexes show intense, high-energy σ and weak, low-energy π ligand-to-metal charge transfer (LMCT) transitions as a consequence of their σ metal–ligand bonding in the ground state. Relative to normal cupric complexes the atypical spectral features of Pc reflect its unusual active site coordination. In particular, in absorption, an inverted CT intensity pattern is observed (i.e. intense, low-energy π and weak, high-energy σ CT transitions, as seen in Fig. 1A), and unusual spin Hamiltonian parameters are observed in the X-band EPR spectrum of Pc (Fig. 1B). Tetragonal (i.e. Jahn–Teller distorted) Cu^{2+} coordination complexes exhibit a large hyperfine coupling ($A_{||} \approx |164| \times 10^{-4}\ cm^{-1}$) of electron and nuclear spin while in the BC sites this coupling is significantly reduced, $A_{||} \approx |63| \times 10^{-4}\ cm^{-1}$. These unique features have been shown to derive from the highly covalent Cu $d_{x^2-y^2}$–S(Cys) π ground state (Fig. 2) [13]. The thioether S(Met) axial ligand interaction is weak at 2.9 Å and is compensated by the strong equatorial S(Cys) ligand. This leads to a π bonding interaction between the thiolate 3p and the $3d_{x^2-y^2}$ orbital of Cu^{2+} and a highly covalent Cu^{2+}–S(Cys) bond. The π bonding nature is responsible for the inverted CT intensity pattern in absorption, and the high covalency reduces the hyperfine coupling of the unpaired electron in the Cu^{2+} derived molecular orbital (MO) because the electron spin density is strongly delocalized onto the thiolate. This MO in Fig. 2 is referred to as the redox active molecular orbital (RAMO) as it accepts and delivers electrons during ET function.

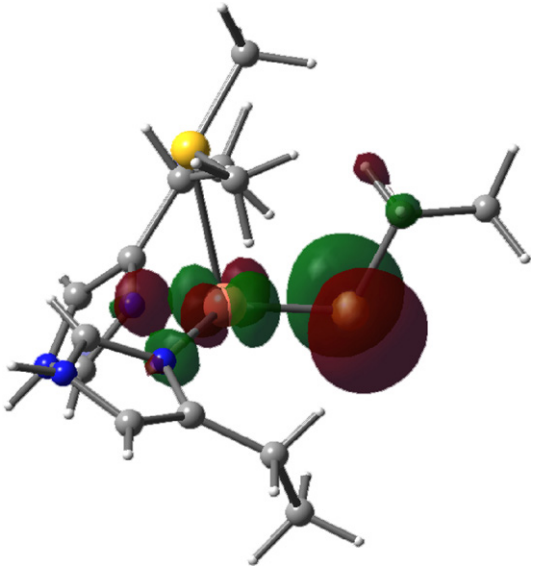

Fig. 2. Ground state wavefunction (β-LUMO) of a T1 BC site.

The BC site has been the subject of several reviews [5,14,15] where, in particular, Ref. [5] covers the contributions of electronic structure to electron transfer reactivity. Here we focus on a few more recent advances concerning specific spectroscopic issues dealing with the assignment of the T1 BC spectral features as well as how changes in these spectral features can be used to understand the entatic state and its contribution to function. First we examine the effects of ligand and metal perturbations on the bonding and spectral features in BC sites using site directed mutants of Cu coordinated S(Cys) and S(Met) ligands [16–18] (done in collaboration with Prof. Y. Lu) and a series of metal-varied BC model complexes [19–21] (done in collaboration with Prof. K. Fujisawa). These studies resolve continued issues concerning the assignment of the unique spectral features of BC proteins and the nature of metal–thiolate bonding. We then focus on the green copper site in nitrite reductase (NiR) [22]. This site has more normal structural and spectral features relative to BC in that the higher energy σ CT transition is intense and the lower energy π CT is weak. This CT intensity pattern gives the protein its green color. This site is also more tetragonally distorted than BC sites with the S(Cys)–Cu–S(Met) plane rotated into the N(His_1)–Cu–N(His_2) plane. It also has a longer Cu^{2+}–S(Cys) bond (~2.21 Å) and shorter Cu^{2+}–S(Met) bond (~2.45 Å). Correlation between the green and BC sites defines the nature of the 'entatic' or 'rack-induced' state in BC proteins such as Pc and its function in tuning E^0 into a physiological range for ET.

2. Active site ligand and metal perturbations

2.1. Ligand perturbations: S → Se

T1 or BC proteins are now well understood from a geometric and electronic structure correlation perspective. A large majority of this understanding has derived from detailed spectroscopic studies. However, particular information elucidated from these spectroscopies has remained assumptive, but can be experimentally evaluated by making well defined structural perturbations.

Here we discuss the spectroscopic insights from a study on the S → Se variants C112SeC and M121SeM of *Pseudomonas aeruginosa* azurin (Az) using a variety of spectroscopies and density functional theory (DFT) calculations [18] in order to quantitatively evaluate the effects of replacing the S(Met) and S(Cys) with Se(Met) and Se(Cys), respectively.

2.1.1. S K-edge X-ray absorption spectroscopy

Ligand K-edge X-ray absorption spectroscopy (XAS) is a powerful technique capable of quantitatively determining the covalency of metal–ligand bonds [23]. A typical S K-edge XAS spectrum contains an intense, higher energy rising edge at ~2474 eV, and, in some cases, a less intense, lower energy feature called the pre-edge at ~2470 eV. The former is a ligand-based, electric dipole allowed S 1s → 4p transition. The latter is assigned to a ligand-based S 1s → metal 3d transition [24]. Since the S 1s orbital is localized on the thiolate and s → p is electric dipole allowed, this transition gains intensity through covalent mixing of S 3p character into the metal 3d orbitals. Thus the intensity of the pre-edge transition is directly proportional to the amount of ligand np character (α^2 in Eq. (1)) mixed into the unoccupied or half-occupied metal-based 3d orbitals of the ground state wavefunction (Ψ^*) due to covalent bonding where α is the S 3p coefficient in the half-occupied Cu^{2+} MO.

$$\Psi^* = (1-\alpha^2)^{1/2}|M3d> - \alpha|Lnp> \quad (1)$$

In addition to the intensity of the pre-edge, this transition contains chemical information in its energy, which is determined by the effective nuclear charge on Cu (Q_{Cu}), the charge on S (Q_S), and the LF environment of Cu. In order to fully quantify the S K-edge spectra of BC sites, the major contributor to this transition must be determined as there are two S ligands coordinated to the Cu ion, S(Met) and S(Cys). This was accomplished using site-directed mutants of Az prepared by Prof. Y. Lu.

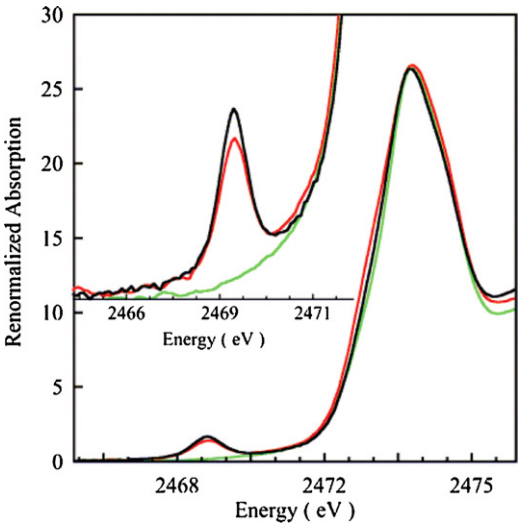

Fig. 3. S K-edge X-ray absorption spectra of WT Az (black line), M121SeM Az (red line), and C112SeC Az (green line). Expanded pre-edge region shown in the inset. Reproduced from Ref. [18] with permission of the American Chemical Society.

The renormalized S K-edge spectra of wild-type (WT) and M121SeM Az are presented in Fig. 3. Both pre-edge features are observed at ~2469 eV. The similarity in energy demonstrates that the LF environment of the Cu as well as the Cu and S active site charges are similar in Az and its M121SeM Az variant. The percent S character from the pre-edge intensity in WT and M121SeM Az are 40 ± 3% and 37.5 ± 3%, respectively. Although within error, the slight decrease in pre-edge intensity could either be due to the increased size of the Se(Met) ligand as compared to S(Met), or the elimination of a possible contribution to the pre-edge intensity from the Cu^{2+}–S(Met) bond. For the former, the increased atomic radius of Se versus S could increase the charge donation of Se(Met) to Cu^{2+}, effectively decreasing the Cu^{2+}–S(Cys) interaction. Extended X-ray absorption fine structure (EXAFS) experiments do indicate a slight lengthening of the Cu^{2+}–S(Cys) bond in M121SeM Az of ~0.04 Å (2.14–2.18 Å) [17]. Considering the latter possibility, the S(Met) could in principle make a limited contribution to the pre-edge intensity. However, this could be ruled out by the S K-edge XAS data of both a model complex, CuL1 (where H_2L1 = 2,6-bis[*S*-(3,5-di-*tert*-butyl-2-hydroxyphenyl)sulfanylmethyl]pyridine) [25], which contains two thioether ligands bound to Cu^{2+}, and the C112SeC Az variant. The S pre-edge feature of CuL1 occurs at ~2472 eV, roughly 3 eV higher in energy (data not shown) than the pre-edge feature of Az and the variant proteins. So, if the S(Met) did contribute to the S K-edge spectra of T1 BC proteins, it would contribute at an energy higher than the pre-edge feature observed at ~2469 eV. This is due to the higher Z_{eff} of the Met which gives a chemical shift of the 1s orbital down in energy, thus increasing its transition energy to the Ψ^* of CuL1. Importantly, the S K-edge spectrum of C112SeC Az (Fig. 3, green line) exhibits no pre-edge feature below 2471 eV. Thus, the intensity of the S K pre-edge for BC proteins does not contain a contribution from the Cu^{2+}–S(Met) bond and is solely reflective of the covalency of the Cu^{2+}–S(Cys) bond, which in Az is then experimentally determined to be 40 ± 3%.

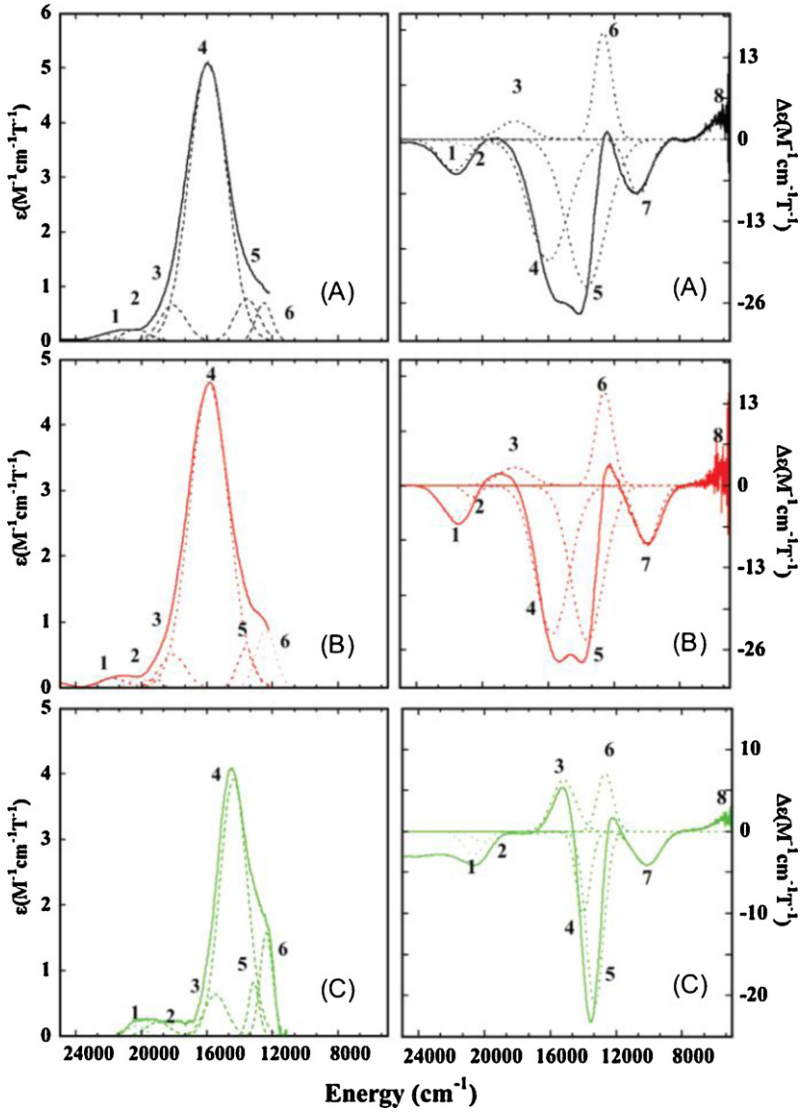

Fig. 4. Electronic absorption and MCD spectra of WT Az (black line), M121SeM Az (red line), and C112SeC Az (green line). Reproduced from Ref. [18] with permission of the American Chemical Society.

2.1.2. Absorption and magnetic circular dichroism spectroscopy

As mentioned in Section 1, the oxidized BC sites such as Pc exhibit unique spectral features relative to normal cupric complexes. An important advance in understanding the electronic absorption spectral features and how they relate to the unusual Cu^{2+} coordination and the resultant electronic structure of BC sites was based on the low temperature (LT) magnetic circular dichroism (MCD) spectrum of Pc [26]. This was crucial in distinguishing between LF and CT transitions and revealed the intense π/weak σ inverted CT intensity pattern characteristic of BC proteins. (Note that, in general for LMCT transitions, the σ CT is intense and the π CT is weak due to the large donor/acceptor orbital overlap involved in σ bonding).

The oxidized BC active site contains a paramagnetic Cu^{2+} ion, and at LT a *C*-term MCD intensity mechanism will dominate. As presented below, this derives from spin-orbit (SO) coupling, and the mechanism can be better understood using the S → Se ligand perturbations where this change leads to a large increase in ligand SO coupling ($\xi_{3p}(S) \approx 382\,cm^{-1}$ versus $\xi_{3p}(Se) \approx 1690\,cm^{-1}$).

LT absorption and MCD spectra of Az and its M121SeM and C112SeC variants are presented in Fig. 4. The absorption and MCD intensities are reported in terms of ε and $\Delta\varepsilon$, respectively. (The absorption and MCD (and LT CD) data for each site was simultaneously fit to one set of Gaussians with the same energy and full width at half maximum (FWHM), but with different amplitudes and signs (for LT MCD and CD) due to the different selection rules involved in each spectroscopic method). The spectra of WT Az and Pc have been shown to be similar and therefore we adopt the band assignment of Pc for that of Az as well as the S → Se variants. From low to high energy, the absorption and MCD spectra of WT Az consist of LF transitions (bands 5–8) and LMCT transitions (bands 1–4). Bands 5–8 have been assigned as the d_{xz-yz}, d_{xz+yz}, d_{xy}, and d_{z^2} to $d_{x^2-y^2}$ LF transitions, respectively. Bands 1–4 have been assigned to the S(Met), His π, S(Cys) σ, and S(Cys) π to Cu^{2+} $3d_{x^2-y^2}$ CT transitions, respectively. Comparison of WT Az and M121SeM Az shows that the energy and intensity of the absorption and MCD transitions do not differ significantly. Furthermore, band 8, assigned as the d_{z^2} → Cu $3d_{x^2-y^2}$ LF transition, which is sensitive to axial ligand interaction with Cu^{2+}, occurs at $5430\,cm^{-1}$ in WT Az and $5410\,cm^{-1}$ in M121SeM Az. Together these data indicate that the electronic structure and Cu–S/Se axial donor interaction does not vary significantly between WT and M121SeM Az.

The absorption and MCD data of C112SeC Az are shown in Fig. 4C. For the most part, the energy and intensity of the LF and LMCT

bands remain similar to those of WT Az. Band 4, the S(Cys) pπ → Cu $3d_{x^2-y^2}$ CT, has now become a Se(Cys) pπ → Cu $3d_{x^2-y^2}$ CT and is red-shifted by ~1700 cm^{-1}, resulting in its overlap with band 5 in the absorption and MCD spectra (Fig. 4C). However, as in WT Az, band 4 still exhibits very similar relative absorption and MCD intensities even with the large change in ligand SO coupling. To understand the S → Se data, we consider the MCD *C*-term intensity mechanisms.

The relative intensities of a transition in absorption and MCD can be taken together and expressed in terms of its C_0/D_0 ratio:

$$\frac{C_0}{D_0} = \frac{kT}{\mu_B B}\left(\frac{\Delta\varepsilon}{\varepsilon}\right)_{max} \quad (2)$$

where *T* is the temperature, *B*, the applied external magnetic field strength, *k*, the Boltzmann constant, μ_B, the Bohr magneton, ε, the absorption maximum in $M^{-1}\,cm^{-1}$, and $\Delta\varepsilon$, the MCD intensity maximum measured in $M^{-1}\,cm^{-1}\,K^{-1}$. The majority of metalloprotein active sites have low symmetry (C_1), and thus contain no orbital degeneracy. For a transition to have non-zero MCD intensity there must be two perpendicular transition moments (for excitation with circularly polarized light). With no orbital degeneracy, all electronic transitions in the BC active site are localized in a single molecular direction, i.e. along a specific metal–ligand bond. Thus SO coupling is required to generate non-zero *C*-term intensity as this can couple excited states with perpendicular electric dipole transition moments. The magnitude of the C_0/D_0 ratio will then depend on the SO coupling parameters for the centers involved in the transition. For atoms in the active site of WT BC proteins, the SO coupling constants are: $\xi_{3d}(Cu) \approx 828\,cm^{-1}$, $\xi_{3p}(S) \approx 382\,cm^{-1}$, and $\xi_{2p}(N) \approx 70\,cm^{-1}$, and because the SO coupling is much larger on Cu than the ligand atoms, the Cu center dominates the *C*-term intensity and leads to intense LF transitions in MCD relative to absorption intensity at LT. However, given that the SO coupling parameter for Se is much larger than for Cu ($\xi_{3p}(Se) \approx 1690\,cm^{-1}$), and that, in the C112SeC Az variant, the S(Cys) pπ → Cu $3d_{x^2-y^2}$ CT transition is now a Se(Cys) pπ → Cu $3d_{x^2-y^2}$ CT transition, it is interesting that there is little change in the MCD C_0/D_0 ratios (from −0.04 in WT Az to −0.02 in C112SeC Az for the Cys pπ → Cu $3d_{x^2-y^2}$ CT transition). This similarity between the MCD spectra of WT Az and its M121SeC and C112SeC Az variants provides further insight into the LT MCD *C*-term intensity mechanism for BC proteins.

In the framework of BC sites such as Pc, Az, and its M121SeM and C112SeC variants, the *z* axis of the molecular and electronic coordinate system lies approximately along the Cu–S(Met) bond vector from single crystal EPR studies [27]. Three ligands are perpendicular to this and are thus in the *x*,*y* plane. The LMCT states associated with these ligands (i.e. the strong S(Cys) and 2 N(His) to Cu $3d_{x^2-y^2}$ CT transitions) will be *x*,*y* polarized along their respective metal–ligand bonds. The C_0-parameter for the MCD intensity for a spin-allowed transition between two non-degenerate states in this coordinate system is then given by [28–30]:

$$C_0 = (A \to J) = (-1/6)\sum_{xyz} g_z \sum_{K \neq A,J} [\Delta_{KJ}{}^{-1} L_z^{KJ}(D_x^{KA}D_y^{AJ} - D_y^{KA}D_x^{AJ}) + \Delta_{KA}{}^{-1} L_z^{KA}(D_x^{AJ}D_y^{JK} - D_y^{AJ}D_x^{JK})] \quad (3)$$

where g_z is the effective *g*-value in the *z*-direction, |*A*> is the ground state, |*J*> is the excited state involved in the transition, |*K*> is an intermediate state, Δ_{ij}'s are the energy differences between states |*i*> and |*j*>, D_k^{ij}'s are the one electron electric dipole transition moments for the |*i*> → |*j*> transition in the *k* direction, and L_z^{ij} is the SO coupling in the *z*-direction between states |*i*> and |*j*>. From Eq. (3) there are two mechanisms which can generate non-zero *C*-term intensity. These are pictorially represented in Scheme 1A and B.

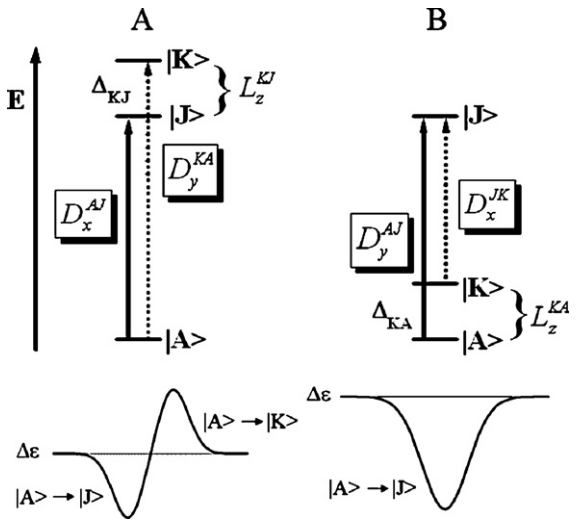

Scheme 1. Two possible MCD C-term mechanisms operative in BC proteins.

In the first term in Eq. (3), MCD intensity derives from SO coupling between two excited states |*J*> and |*K*> that are close in energy. They are both associated with orthogonal *x*,*y* polarized transitions from the ground state. The second mechanism generates MCD intensity by SO coupling between the ground state |*A*> and a low-lying, intermediate excited state |*K*> from which two orthogonal *x*,*y* polarized transitions can be made to a single excited state |*J*>. Mechanism one results in a pseudo-A term made up of two oppositely signed *C*-terms with equal intensities (Scheme 1A). The second mechanism leads to a deviation from the MCD sum rule (i.e. more intensity in one circular polarization summed over the excited states) (Scheme 1B). From Fig. 4 the MCD spectra of BC proteins have comparable contributions from both mechanisms.

x,*y* polarized LMCT transitions from the N(His) and S(Cys) ligands involve two different donor orbitals (i.e. S(Cys) π and N(His) π) and the same acceptor orbital (i.e. Cu^{2+} $3d_{x^2-y^2}$). Importantly, the SO coupling operator is a dominantly single center, one electron operator. Therefore, in mechanism one L_z^{KJ} is required to be metal centered as this is the only atom contributing to both the donor orbitals of the Cys and the His based CT transitions. The S(Cys) CT transition leaves a hole in the thiolate π bonding orbital which has $3d_{x^2-y^2}$ character and the N(His) CT leaves a hole in the His π bonding orbital which has $3d_{xy}$ character. L_z^{KJ} transforms as a rotation about the *z*-axis and will SO couple these associated CT exited states. A similar metal centered behavior is operative for mechanism two (Scheme 1B) where the d_{xy} LF excited state can SO couple into the $d_{x^2-y^2}$ ground state. Thus, the LT MCD data on Az and the M121SeM and C112SeC Az variants confirm that the *C*-term intensity mechanism for BC sites is derived dominantly from metal d character, and this leads to the very similar MCD behavior even upon a large increase in ligand SO coupling.

2.1.3. Resonance Raman spectroscopy

Laser excitation into the ~600 nm S(Cys) pπ → Cu^{2+} $3d_{x^2-y^2}$ CT transition of the BC proteins results in complex rR spectra in the region of ~250–500 cm^{-1} (Fig. 5, left) [31–42]. Initially one might expect to see one vibration in the 400 cm^{-1} region associated with the Cu^{2+}–S(Cys) unit as rR intensity drives from excited state distortion, and this transition involves excitation of a Sπ–dπ bonding electron into its antibonding counterpart, which should elongate the Cu–S bond. However, X-ray crystal structures of BC proteins show Cu–S_γ–C_β–C_α and S_γ–C_β–C_α–N dihedral angles of ~170°, and it has been suggested that this structural constraint results in the coupling the Cu^{2+}–S(Cys) stretch with deformation modes of the

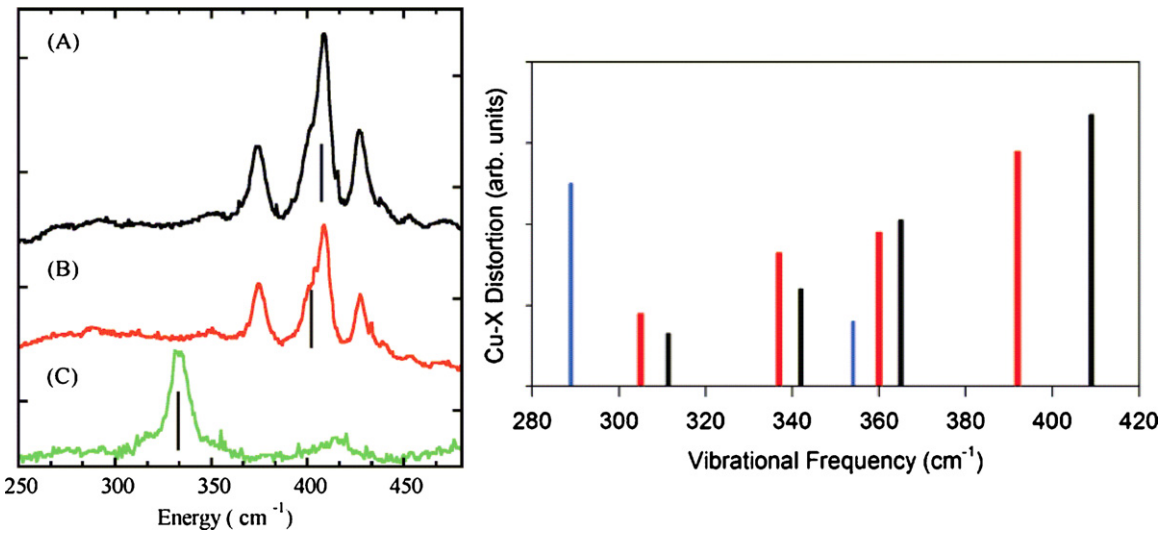

Fig. 5. Left: rR spectra of (A) WT Az, (B) M121SeM Az, and (C) C112SeC Az. Right: DFT calculated Cu–S mixing into normal modes for [(tpz)Cu(SC_6F_5)]; X = S (black line), X = Se (blue line), X = ^{32}Se (red line).
Reproduced from ref. [18] with permission of the American Chemical Society.

S(Cys) ligand [43,44]. As a gauge of bond strength, the intensity weighted (I) frequency distribution (ν) of the vibrational features (i) observed in the energy region of metal–ligand stretching in the rR spectrum are used to calculate an effective vibrational frequency of the Cu^{2+}–S(Cys) bond, <νCu–S(Cys)> [41]:

$$< \nu\text{Cu–S(Cys)} >= \frac{\sum_i[(I^i_{01})(\nu_i)^2]}{\sum_i(I^i_{01})(\nu_i)} \quad (4)$$

Fig. 5, left shows the rR spectra of WT Az and its C112SeC and M121SeM variants. The structured rR spectrum of M121SeM remains very similar to that of the WT protein with only a slight decrease in <νCu–S(Cys)> from 407 to 402 cm^{-1}, consistent with the slight decrease in the intensity of the S K pre-edge feature, and is due to the slight increase in Cu^{2+}–S(Cys) bond length for M121SeM relative to WT Az. Interestingly, the rR spectrum of C112SeC Az shows drastically different behavior in that the complex spectral pattern has been reduced to a lone feature at 333 cm^{-1}.

DFT based frequency calculations on a model complex, [(tpz)Cu(SC_6F_5)], have been used to elucidate the origin of the rR spectral perturbations for C112SeC Az (Fig. 5, right). In [(tpz)Cu(SC_6F_5)] [19] the Cu–S distortion has a potential energy distribution (PED) that is calculated to be dispersed over four normal modes in the 300–400 cm^{-1} region (multiple features are observed in the experimental rR for this model complex) [21], similar to the rR spectrum of WT Az. However, when S is replaced with Se in the DFT geometry optimization, the resulting frequency calculation yields a PED where the Cu^{2+}-Se distortion collapses into a single normal mode with an energy of ~290 cm^{-1}, in good agreement with the rR behavior of the C112SeC Az variant (Fig. 5, left). This would either reflect a mass effect or differences in bonding between S(Cys) and Se(Cys) and Cu^{2+}, so the hypothetical Cu^{2+}–^{32}Se vibrational calculation was also performed. This mass change restores the coupling of the Cu^{2+}–^{32}Se distortion into a distribution over four modes. These results indicate that replacing S with Se raises the mass of the ligand and thus lowers the metal–ligand stretching frequency, shifting it out of the energy range appropriate for mechanical coupling with the ligand deformation modes now at higher energy. This confirms that the structured rR spectra of BC sites reflect kinematic coupling of the Cu^{2+}–S(Cys) stretch with deformation modes of the thiolate ligand. Spectral changes in this energy region reflect the coupling of the Cu^{2+}–S(Cys) stretch with protein modes, and serves as a direct probe of protein structural changes in the vicinity of the BC site [45].

2.2. Metal perturbations: Mn → Zn

Clearly, from preceding sections, we have a rigorous understanding of the bonding description and associated electronic structure of BC sites. Here, we use this to further understand how metal–thiolate bonding changes with the nature of the metal ion through a study on a series of metal-varied model complexes with structures and spectra similar to metal substituted BC proteins [46–55]. These crystallographically characterized complexes of Prof. K. Fujisawa are of the general formula [$ML(SC_6F_5)$] where L = $HB(3,5\text{-}^{i}Pr_2pz)_3^-$ (pyrazolyl (pz)) and M^{2+} = Mn, Fe, Co, Ni, Cu, and Zn [19,20]. In these complexes, the metal ion is in a distorted T_d coordination environment made up of two equatorial M–N bonds, one slightly elongated axial M–N bond from the tris-pz ligand, and a fourth $S_{thiolate}$ is bound equatorially. As observed for the BC proteins, metal–thiolate bonding generates the dominant spectral features in these complexes.

The thiolate ligand has three valence 3p orbitals available for bonding, two of which are at an energy suitable for forming metal–ligand bonds. The other interacts strongly with the C–S σ bond and is thus stabilized in energy. The two bonding valence 3p orbitals are perpendicular to the C–S bond and are capable of forming either a π bond (orbital out of the C–S–M plane) or a pseudo-σ bond (in-plane). The pseudo-σ bonding description of the latter orbital reflects the C–S–M angle as its overlap with metal d orbitals shifts off-axis as the C–S–M angle becomes greater than 90°. In BC sites, this angle ranges from 100 to 120° and is similar in these complexes.

In the following sections we focus on the spectroscopic trends across the metal–thiolate series and relate these differences to important variations in bonding using experimentally validated DFT and time-dependent DFT (TD-DFT) calculations [21].

2.2.1. Charge transfer spectroscopy and covalent bonding

The electronic absorption data for the divalent metal series is shown in Fig. 6 and were assigned using a combination of MCD (to differentiate CT from LF transitions) and rR (to define thiolate π and σ CT transitions) in Ref. [21]. Interesting trends in the CT transitions provide insight into the covalent interactions between

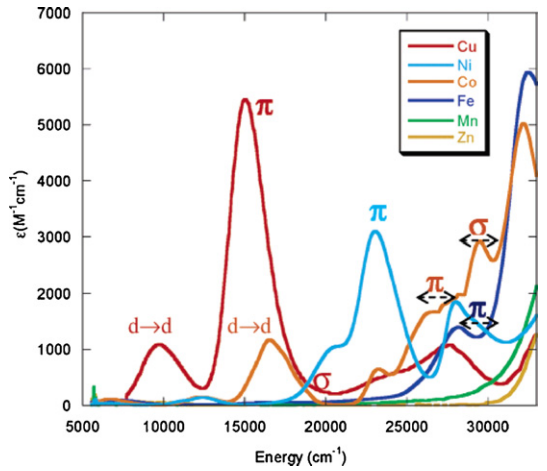

Fig. 6. Electronic absorption spectra of the [ML-(SC_6F_5)] complexes. Reproduced from Ref. [21] with permission of the American Chemical Society.

the metal and the thiolate ligand. TD-DFT calculations using a B3LYP exchange correlation functional and a large basis set (6-311+G*) reproduce the absorption spectral data well, and confirm the band assignments (Fig. 7). The Zn complex, being d^{10}, shows no absorption in the visible region of the spectrum. However, in the d^9 Cu complex an intense absorption feature is observed at ~15,000 cm^{-1}, which is assigned as a $S_{thiolate}$ $p\pi \rightarrow Cu^{2+}$ $3d_{x^2-y^2}$ transition. This reproduces the well defined absorption spectrum of the BC proteins and reflects the high anisotropic covalency (of the π type) of the Cu^{2+}–$S_{thiolate}$ bond (*vide supra*). The Ni complex also shows an intense absorption feature in the visible region that

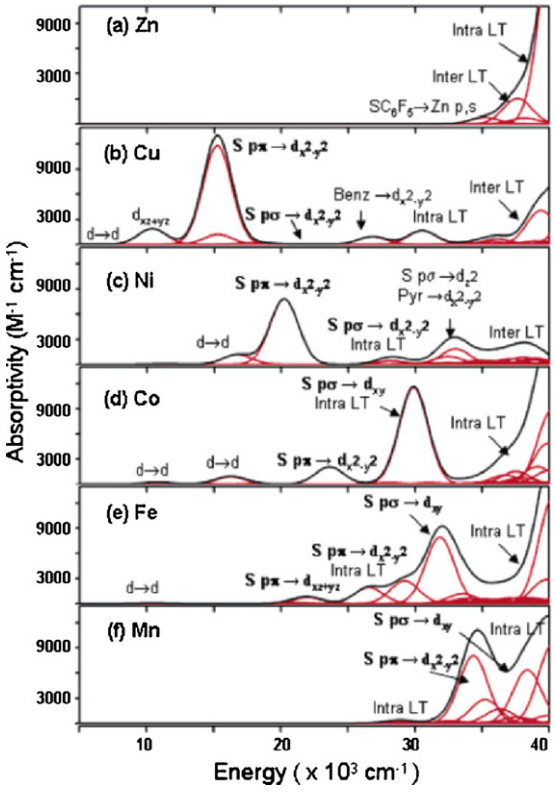

Fig. 7. Simulated TD-DFT calculated electronic absorption spectra of the [ML-(SC_6F_5)] complexes with individual contributions (Gaussian functions with FWHM of 2500 cm^{-1}) shown in red.
Reproduced from Ref. [21] with permission of the American Chemical Society.

is blue shifted to ~20,000 cm^{-1}, ~5,000 cm^{-1} higher in energy than the Cu complex and less intense (ε = 8000 versus 12,000 M^{-1} cm^{-1}). This band is also assigned as a $S_{thiolate}$ $p\pi \rightarrow Ni^{2+}$ $3d_{x^2-y^2}$ transition. There is also a weaker $S_{thiolate}$ $p\sigma \rightarrow Ni^{2+}$ $3d_{x^2-y^2}$ transition located at ~28,000 cm^{-1}. In the Co complex, a $S_{thiolate}$ $p\pi \rightarrow Co^{2+}$ $3d_{x^2-y^2}$ transition is also observed, blue shifted by ~4,000 cm^{-1} relative to the π CT of the Ni complex, at ~24,000 cm^{-1} and again less intense ($\varepsilon \sim 3000\ M^{-1}\ cm^{-1}$). More interesting is the appearance of a new, intense ($\varepsilon \sim 11{,}000\ M^{-1}\ cm^{-1}$) absorption feature at ~30,000 cm^{-1}. Relative to the Ni and Cu complexes, in the Co complex the $3d_{xy}$ orbital is now vacant, and strongly interacts with the $S_{thiolate}$ pσ orbital, allowing for a $S_{thiolate}$ $p\sigma \rightarrow Co^{2+}$ $3d_{xy}$ CT transition. Thus, the intensity of the $S_{thiolate}$ pπ and $S_{thiolate}$ pσ CT transitions is reversed beginning with the Co complex (i.e. σ CT now more intense than π CT) as the acceptor orbital is now $3d_{xy}$ with lobes along the M–$S_{thiolate}$ bond. This is likewise observed for the Fe and Mn complexes. Going from Co to Fe, the $S_{thiolate}$ $p\sigma \rightarrow Fe^{2+}$ $3d_{xy}$ transition decreases in intensity ($\varepsilon \sim 8000\ M^{-1}\ cm^{-1}$) and is blue shifted to ~32,000 cm^{-1}. Finally, for the Mn complex, the $S_{thiolate}$ $p\pi \rightarrow Mn^{2+}$ $3d_{x^2-y^2}$ and the $S_{thiolate}$ $p\sigma \rightarrow Mn^{2+}$ $3d_{xy}$ CT transitions are located at ~35,000 and ~38,000 cm^{-1}, respectively.

The trends in the absorption data and TD-DFT calculated spectra thus show that: (1) the $S_{thiolate}$ $p\pi \rightarrow M^{2+}$ $3d_{x^2-y^2}$ CT transition shifts to higher energy and decreases in intensity from Cu → Ni → Co, and (2) an intense $S_{thiolate}$ $p\sigma \rightarrow M^{2+}$ $3d_{xy}$ CT appears for the Co complex and shifts to higher energy and decreases in intensity in going from Co → Fe → Mn. We analyze the ground state DFT calculations to further understand these spectral differences and how they relate to metal–thiolate bonding.

Fig. 8A shows the energy level diagram for the relevant β-spin frontier MOs of the metal series while Fig. 8B shows contour plots of the major metal–thiolate π ($S_{thiolate}$ $p\pi/Cu^{2+}$ $3d_{x^2-y^2}$ interaction, left) and σ ($S_{thiolate}$ $p\sigma/Cu^{2+}$ $3d_{xy}$ interaction, right) bonds. Several important points are illustrated in the energy diagram. In the Mn complex, all of the β-spin 3d orbitals are unoccupied, and energetically well separated from occupied MOs.

In the Fe complex, the β-spin d_{yz-xz} orbital is now the HOMO and the β-HOMO-LUMO gap is lowered by ~3.7 eV. This energy decrease is due to the increased Z_{eff} of Fe relative to Mn. The consequence of increased Z_{eff} is increased metal–thiolate covalency due to the energetic stabilization of the 3d manifold, which increases the 3d-thiolate orbital interaction.

The Co complex has an additional electron in the d_{yz+xz} orbital, and the β-HOMO-LUMO gap decreases relative to Fe. In the Co complex the bonding interaction between the $S_{thiolate}$ pσ orbital and the low-lying unoccupied d_{xy} orbital (Fig. 8B) becomes stronger due to increased Z_{eff}, which gives an additional strong σ component to the Co^{2+}–$S_{thiolate}$ bond (Fig. 8B, right). This will be correlated to the results of a Mayer bond order analysis (*vide infra*).

The additional electron in the Ni complex fills the d_{xy} orbital. This eliminates the strong σ bonding component present for $Co^{2+} > Fe^{2+} > Mn^{2+}$.

The d_{z^2} orbital becomes occupied in the Cu complex, leaving a single hole in the $d_{x^2-y^2}$ orbital. This allows for a strong π type interaction between the Cu $3d_{x^2-y^2}$ and thiolate 3p orbital (Fig. 8B, left). The strong orbital overlap and further increase in Z_{eff} both contribute to the increased covalency of the Cu complex, making it the most covalent of the metal series with the most intense CT features.

The covalent contributions to bonding were further evaluated using Mayer bond orders [56–59], $\mathbf{B}_{AB}$ (A and B are metal and ligand components, respectively), which were decomposed into α- and β-spin orbital components [21]. The results of the Mayer bond order analysis are presented in Fig. 9A. The π-type Mayer bond orders from the α-spin MOs, $\mathbf{B}^{\alpha}$M–S(π), are close to zero for all

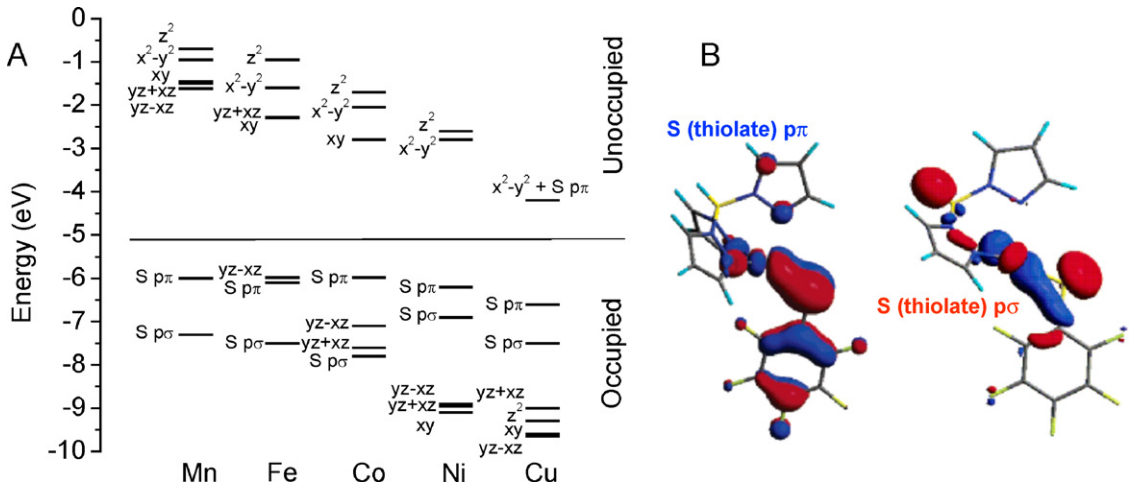

Fig. 8. (A) β-Spin frontier molecular orbital energy diagram of the [ML-(SC_6F_5)] complexes. (B) Representative contour surfaces of the S(thiolate) pπ (with $d_{x^2-y^2}$) and pσ (with d_{xy}) frontier molecular orbitals of the [ML-(SC_6F_5)] complexes.
Adapted from Ref. [21].

complexes due to the fact that the α set of 3d orbitals is fully occupied across the series. The $\mathbf{B}^{\alpha}$M–S(σ) components to the Mayer bond orders arise from the interaction of the ML^+ LUMO (~80% M 4 s character) and the thiolate fragment HOMO-1 (S pseudo-σ). This interaction is consistent across the series (Fig. 9A). The β-spin contributions to the Mayer bond orders, however, do show important changes due to variable occupation of the β 3d orbitals. These variations produce changes in the covalent contribution to bonding. The $\mathbf{B}^{\beta}$M–S(σ) component becomes a major contributor to the overall bond order in Co^{2+}. This parallels the above analysis in that there is a strong bonding interaction between the $S_{thiolate}$ pσ orbital and the low-lying unoccupied $3d_{xy}$ orbital, which results in an intense σ CT transition. The $\mathbf{B}^{\beta}$M–S(σ) component decreases from Co^{2+} to Fe^{2+} to Mn^{2+} (Fig. 9A). The $\mathbf{B}^{\beta}$M–S(π) component increases from Mn^{2+} to Cu^{2+} where a global maximum occurs. This reflects the strong π type interaction between the low-lying, unoccupied Cu $d_{x^2-y^2}$ and the thiolate 3p orbitals and results in an intense π CT transition. This behavior of the separate β-spin σ and π components gives rise to the overall trend in the M–S bond orders (Fig. 9A, top). The changes in covalency and bond order correlate to the trends observed in the CT spectra. The decreased covalency going from Cu → Ni → Co reflects the increase in energy and decrease in intensity of the $S_{thiolate}$ pπ → M^{2+} $3d_{x^2-y^2}$ CT. Similar changes in bonding are associated with the analogous behavior of the $S_{thiolate}$ pσ → M^{2+} $3d_{xy}$ CT in going from Co → Fe → Mn.

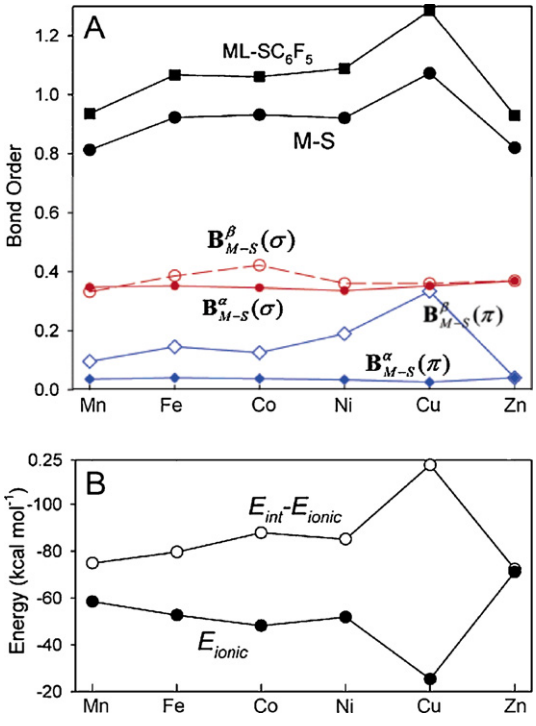

Fig. 9. (A) Mayer M–S bond order (solid black circles), its σ and π components (in red and blue, respectively), and the bond order between the ML^+ and $SC_6F_5^-$ fragments (solid black squares) in the [ML(SC_6F_5)] complexes. (B) E_{ionic} and $E_{int} - E_{ionic}$ components of the ML^+-$SC_6F_5^-$ complex binding energy.
Adapted from Ref. [21].

2.2.2. Ionic versus covalent contributions: the compensation effect

The binding energy, E_0, between the ML^+ and $SC_6F_5^-$ fragments can be partitioned as in Eq. (5):

$$E_0 = E_{int} + E_{prep} \quad (5)$$

where E_{int} and E_{prep} are the interaction and preparation energy, respectively. The latter is the energy cost to transform the ML^+ and $SC_6F_5^-$ fragments from their equilibrium geometries and electronic ground states to those of the complexes and varies from 5.3 to 10.3 kcal mol^{-1} for the ML^+ fragment and 1.0 1.2 kcal mol^{-1} for the $SC_6F_5^-$ fragment. We focus on E_{int}, which can be further partitioned:

$$E_{int} = E_{cov} + E_{ionic}. \quad (6)$$

E_{cov} is the covalent interaction energy and E_{ionic} is the ionic electrostatic energy of interaction between the oppositely charged ML^+ and $SC_6F_5^-$ fragments. The formulation and determination of E_{ionic} is presented in Ref. [21].

The X-ray crystallographic and calculated M–S bond distances as well as the calculated binding and interaction energies and force constants are shown in Fig. 10. The DFT calculated M–S bond lengths reproduced the nonmonotonic changes observed in experiment (Fig. 10A); however, when compared to the binding energy (Fig. 10B) there is no clear correlation between the two. The trends in the calculated force constants (Fig. 10C) more closely resemble the changes in bond length. Furthermore, the analysis presented above showed that the largest Mayer bond orders were observed for Co^{2+} and Cu^{2+} because of the dominant contributions from σ and π bonding, respectively (Fig. 9A). However, when one compares the

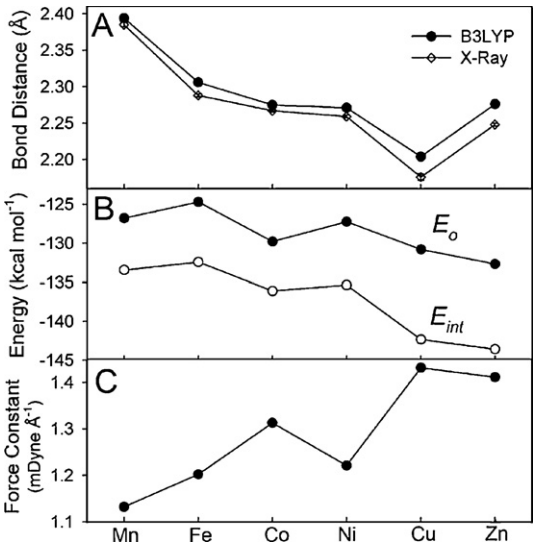

Fig. 10. (A) Experimental and calculated M–S bond lengths and (B) calculated binding energies, E_0, in the [ML-(SC_6F_5)] complexes, (C) calculated M–S force constants. Adapted from Ref. [21].

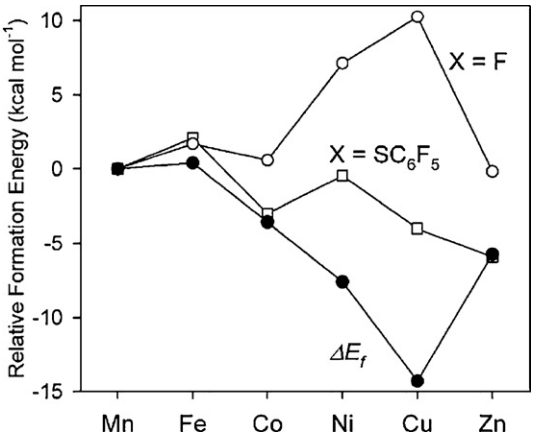

Fig. 11. Relative formation energies, E_f (kcal mol^{-1}), of the metal–thiolate complex, [ML-(SC_6F_5)], and metal–fluoride complexes, [ML-(F)], and their difference, ΔE_f. Reproduced from Ref. [21] with permission of the American Chemical Society.

Mayer bond orders to the binding energies, there is again no direct correlation. For example, the most negative binding energy is calculated for Zn^{2+} (Fig. 10B), yet the highest bond order is for Cu^{2+}. When the ionic term, E_{ionic}, is removed from the total interaction energy as $E_{int} - E_{ionic}$, the result is an estimate of E_{cov}. This is given in Fig. 9B. The term $E_{int} - E_{ionic}$ follows the trend in the bond orders (Fig. 9A) with maxima at Co (σ) and Cu (π). The ionic contribution makes up ~44% of the metal–thiolate interaction energy for the Mn^{2+} complex and 50% for the Zn^{2+} complex while contributing less to the more covalent Co^{2+} (σ type bonding) and Cu^{2+} (π type bonding) complexes.

Thus, the ionic component is also a major contributor to bonding in these complexes. However, from the above discussion the covalent term is a major contributor to the spectral features, and it is the interplay between the two contributions that results in the limited variations in the bonding across the M^{2+}–$S_{thiolate}$ series. That is, even though the increased Z_{eff} increases the covalency of the M–S bond by stabilizing the metal 3d orbitals, this occurs at the cost of contracted metal–ionic radii. If the M–S covalency remained constant, this contraction would cause an increased ionic contribution to bonding. However, increased M–S covalency diminishes the ionic contribution because of an increased charge donation from the $SC_6F_5^-$ to the ML^+ fragment. Thus, covalency lessens the negative charge on the $S_{thiolate}$ and the positive charge on the metal center. Charge donation reduces the ionic contribution to the bond energy, creating a situation where there is a *compensation effect*, wherein increased covalency leads to a decreased ionic term. The similar magnitude and competition between ionic and covalent contributions results in little variation in the M–S binding energy across the series (summarized in Fig. 11, X = SC_6F_5 plot).

2.2.3. The Irving–Williams series

The Irving–Williams series reflects both the ionic and covalent contributions to M–L bonding discussed above and explains the increasing stability constant of complexes of divalent metal ions of the first transition series with increasing atomic number where a maximum is achieved at Cu [60–62]. Fig. 11, X = SC_6F_5 shows that when the calculated metal–thiolate binding energies of these divalent complexes are plotted against atomic number, the result is a clear deviation from the Irving–Williams series. The actual calculated binding energies in Fig. 10B vary from −126.8 kcal mol^{-1} for Mn, to −130.8 kcal mol^{-1} for Cu, and to −132.7 kcal mol^{-1} for Zn. As discussed above, this arises from the compensation effect of comparable contributions from both the ionic and covalent terms in metal–thiolate bonding. The experimental stability constants, however, reflect the competition of this ligand with coordinated solvent (H_2O, OH^-). To avoid H-bonding complications, a F^- was considered as an innocent analogue of an H_2O derived ligand in Ref. [21].

Because of the ionic nature of the metal–ligand bonding in the fluoride series, the trends in covalency then serve to modulate this ionic term, leading to the X = F^- trend in Fig. 11. Here, the ionic term decreases due to increases in covalency from Co → Ni → Cu. The difference in the relative formation energies for the fluoride and thiolate ligands can be taken as:

$$\Delta E_f = [E_0(ML^+ - SC_6F_5^-) - E_0(MnL^+ - SC_6F_5^-)] - [E_0(ML^+ - F^-) - E_0(MnL^+ - F^-)]. \quad (7)$$

The ΔE_f plot in Fig. 11 shows the progression Mn ≈ Fe > Co > Ni > Cu < Zn, which is the Irving–Williams series.

Thus, in the case of the soft thiolate ligand, little absolute change in binding energy is observed due to the compensation effect. Whereas, for the harder, less electron donating ligand, F^-, the small changes in metal–ligand covalency serve to modulate the dominantly ionic binding energy. The contrasting behaviors in metal–ligand bonding between the fluoride (representative of the solvent being replaced) and thiolate result in the Irving-Williams series (solid circles in Fig. 11).

Having rigorously defined the origin and assignment of spectral features of T1 BC sites using ligand and metal perturbations, we use these spectral features and their changes to define the 'entatic' or 'rack-induced' state in the next Section.

3. The nature of the 'entatic' or 'rack-induced' state

We now shift focus to function and present recent studies of two perturbed T1 sites (T1 is used here more generally for sites that have the same ligand set as Pc but can have perturbed spectral features as, indeed, the T1 site in nitrite reductase (NiR) is green): that of *Paracoccus pantotrophus* pseudoazurin (Paz) and that of *Rhodobacter sphaeroides* NiR. These allow the definition of the nature of the 'entatic' or 'rack-induced' state in BC proteins.

A large research effort has been put forth in determining the role of the axial ligand in T1 BC proteins [5,17,63–65]. For those T1 BC sites possessing a thioether ligand, the unusually long Cu–S(Met) bond has been thought to be imposed by the protein matrix. X-ray

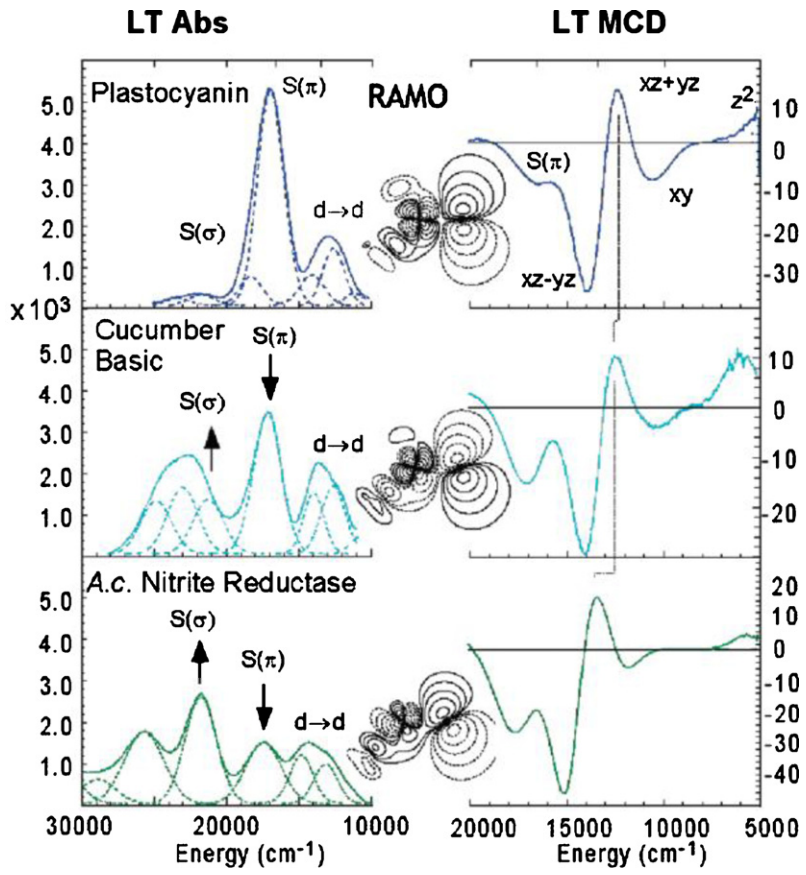

Fig. 12. (Left) Low temperature absorption showing redistribution of the spectral intensity from S(Cys) π to σ charge transfer bands. (Middle) Redox-active molecular orbitals calculated with SCF-Xα-SW showing rotation from a π-type interaction in plastocyanin to a σ/π mixture in nitrite reductase. (Right) MCD spectra showing a shift in the ligand field transtions to higher energy along the coupled distortion coordinate (i.e. tetragonal distortion).
Reproduced from Ref. [100] with permission of the American Chemical Society.

crystallographic data show that, in Pc, this bond is ~2.9 Å in the reduced site [66], which is significantly longer than the majority of Cu^{+}–thioether bonds at ~2.3 Å [67,68]. Decreasing the S(Met) interaction with the Cu center leads to an increased donor interaction from the equatorial S(Cys). This combination of a weak axial S(Met) and strong equatorial S(Cys) removes all orbital degeneracy, thus eliminating the Jahn–Teller distortion that would occur upon oxidation to the orbitally degenerate ground state of the initially T_d cupric site.

Insight concerning the coupling of the geometric to the electronic structure of the BC active sites has been obtained from earlier spectroscopic studies of a series of T1 centers that all have the S(Cys), S(Met), and 2 N(His) ligand set but vary from blue (Pc) to green (NiR) in color due to differences in their electronic absorption spectra (Fig. 12) [69]. A result of these studies was the coupled distortion model [69,70] that explains the variations in spectroscopic properties across this series. Three major geometric changes occur along this coordinate in going from a blue to a green site: (1) a decrease in the Cu^{2+}–S(Met) bond length; (2) increased Cu^{2+}–S(Cys) bond length; and (3) a distortion from a T_d structure to a more tetragonal structure, reflecting a Jahn–Teller (e_u) rotation of the S(Cys)–Cu^{2+}–S(Met) plane toward the N(His_1)–Cu^{2+}–N(His_2) plane. Accompanied with these structural changes are specific spectroscopic changes that include: (1) an increased $\varepsilon_{450}/\varepsilon_{600}$ ratio (i.e. an increase in the S(Cys) $\sigma \rightarrow Cu^{2+}$ $3d_{x^2-y^2}$ CT relative to π CT intensity) due to increased σ character in the ground state wavefunction shown in the middle of Fig. 12; (2) a weaker Cu^{2+}–S(Cys) bond and a decreased effective vibrational frequency in rR, ⟨νCu–S(Cys)⟩; and (3) increased LF transition energies (Fig. 12, right).

T1 Cu sites have been the subject of a number of computational studies. In one of these reports it was questioned whether there is a protein constraint on the oxidized site, leading to the notion that there could be two or more T1 sites existing as energy minima [71]. Using a truncated model (SCH_3, 2 imidazole, $S(CH_3)_2$), two electronic minima were found with similar energies; one exhibiting the geometry of a blue site, the other a green site (note that changing the amount of Hartree–Fock mixing in the density functional leads to one minimum [5]). Experimentally, a limited temperature dependence of the absorption spectrum was found for an amicyanin (Am) loop mutant [72]. This temperature dependence was interpreted as a Boltzmann population of two electronic minima; one blue (maximum absorption at ~600 nm), the other green (maximum absorption at ~450 nm). Below we address these conflicting notions concerning T1 Cu sites, and from experimental and computational data, define the nature of the 'entatic' or 'rack-induced' state in BC proteins like Pc.

3.1. Non-temperature dependent perturbed Type 1 Cu sites

Paz is an interesting T1 BC protein that has an absorption spectrum with significant intensity in both the 450 and 600 nm regions [73,74]. The two absorption features could be due to a single T1 Cu site midway along the coupled distortion coordinate with a mixed π/σ ground state or a mixture of two T1 sites; one green, one blue. Temperature dependent absorption and rR as well as LT multifrequency EPR experiments on Paz resolved this issue.

Fig. 13 (solid line) shows the LT (5K) absorption spectrum of Paz. Two distinct spectral features are observed in the regions of 450

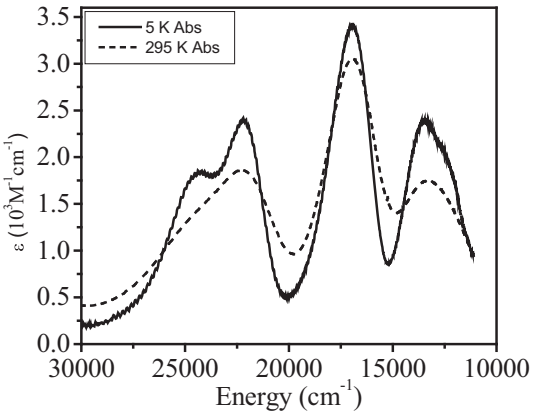

Fig. 13. Electronic absorption spectra of pseudoazurin at 5 K (solid) and 295 K (dashed) K.
Adapted from Ref. [74].

and 600 nm. The energy and intensity pattern is consistent with other perturbed T1 sites such as cucumber basic protein (CBP) [69]. As indicated above, this pattern could be due to a mixture of two sites or a single site with a mixed π/σ ground state wavefunction. rR experiments with laser excitation into both absorption features allowed evaluation of the possibility of a mixture of sites. Fig. 14 shows the resultant rR spectra using laser excitation into both the low (593 nm) and the high energy (450 nm) CT features. As in the rR spectrum of WT Az (Fig. 5A) a large number of resonance enhanced vibrational features are observed, reflecting the kinematic coupling of the Cu^{2+}–S(Cys) stretch with distortion modes of the thiolate at similar energy. The resonantly enhanced vibrations observed for both wavelengths of laser excitation have identical frequencies. The only spectral difference is a redistribution of rR intensity. The effective vibrational frequency, ⟨νCu-S(Cys)⟩, of the Cu^{2+}–S(Cys) bond in Paz obtained with 593 nm excitation is 396 cm^{-1}. Previous rR measurements have yielded values of 413, 403, 394, and 388 cm^{-1} for the T1 sites in fungal laccase, Pc, CBP, and NiR, respectively. The rR data indicate that, for Paz, there is a single species present at LT, which exhibits both σ and π CT absorption intensity. Also interesting is that the rR profiles of these two spectral regions show very different behavior. The lower energy vibrational features (~340–400 cm^{-1}) are more strongly enhanced in the σ CT whereas the higher energy vibrations are only weakly enhanced by the π CT. This suggests that there is a differential electronic coupling mechanism (through different excited state distortions) of the Cu^{2+}–S(Cys) stretch and vibrational modes of the thiolate for the π versus σ CT transitions. In terms of function, the ET process is modulated by the anisotropic covalency of metal–ligand bonds, and differences in the rR spectra for σ and π CT suggest that T1 Cu sites could electronically couple differently into the protein through σ versus π ET pathways.

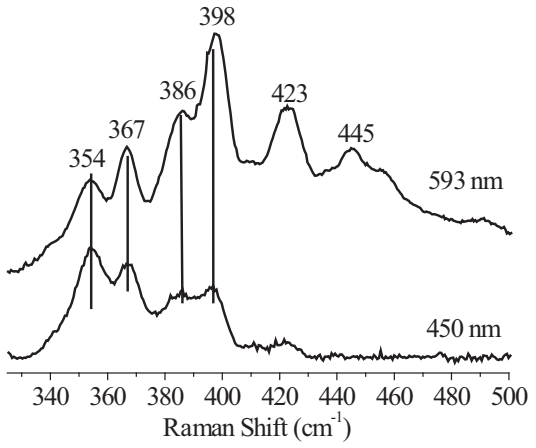

Fig. 14. Resonance Raman spectra of pseudoazurin with laser excitation at 593 and 450 nm at 77 K.
Adapted from Ref. [74].

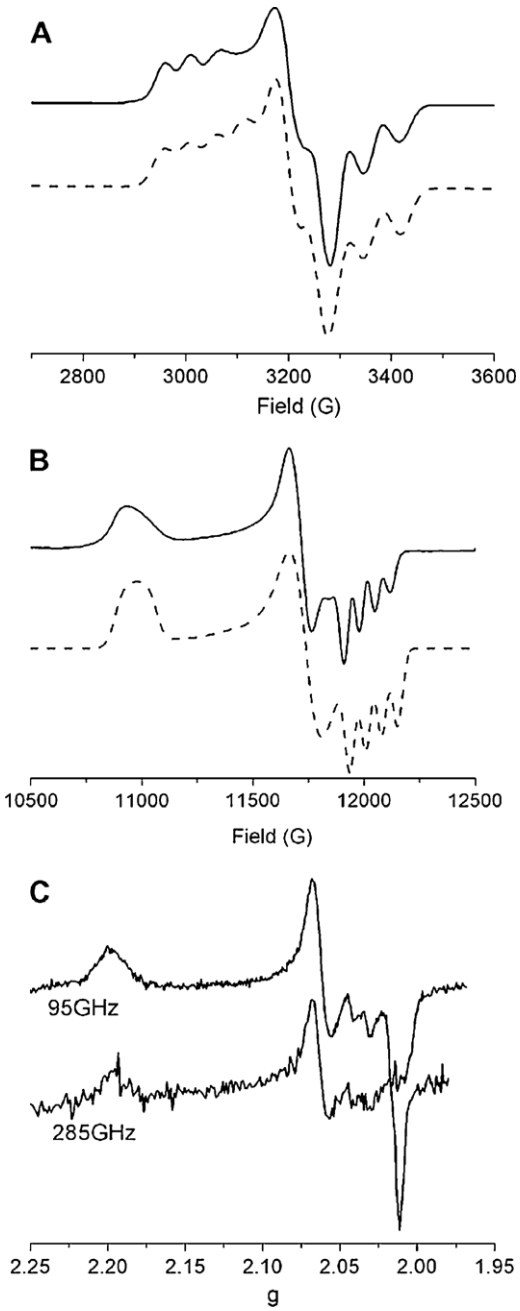

Fig. 15. (A) X-Band and (B) Q-band EPR data on pseudoazurin (solid line: experiment; dashed line: simulation); (C) high frequency EPR data 95 GHz and 285 GHz. Experimental conditions: X-band data, 9.39 GHz, were taken at 77 K; Q-band, 33.83 GHz, were taken at 50 K, EPR spectra at 95 GHz and 285 GHz were recorded at 4.2 K.
From Ref. [74].

As a further indication of a single T1 species at LT, multifrequency EPR data were obtained (Fig. 15). Both X- and Q-band EPR data were simulated using identical spin Hamiltonian parameters, and the high-field spectrum shows a single set of g-values (g_z = 2.200, g_y = 2.065, and g_x = 2.014). These EPR spectral data cor-

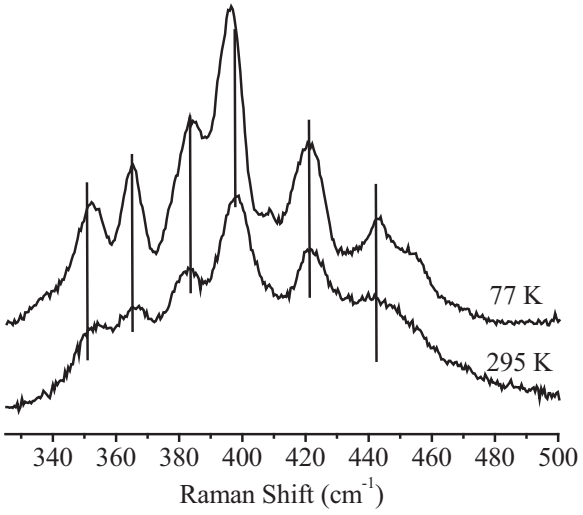

Fig. 16. rR spectra of Paz with laser excitation at 607 nm at 77 and 295 K. From Ref. [74].

roborate the rR data and further confirm the presence of a single species at LT. *The observation of both π and σ CT transitions in an individual species indicates that the BC site in Paz is midway along the blue to green coupled distortion coordinate and is not a mixture of species*.

An overlay of the 5 and 295 K absorption spectra of Paz is given in Fig. 13. Spectral broadening of absorption bands occurs upon increasing the temperature from 5 to 295 K. This is the standard temperature dependence of absorption band shapes for all electric dipole allowed transitions and is related to the thermal population of vibrations involved in the Gaussian band shape. The energy of the band maxima do not change. Importantly, the ratio of total intensity does not change significantly ($(\varepsilon_\sigma/\varepsilon_\pi)_{5K} = 0.70$ and $(\varepsilon_\sigma/\varepsilon_\pi)_{295K} = 0.62$ where σ and π denote the S(Cys) $\sigma \rightarrow Cu^{2+}$ $3d_{x^2-y^2}$ and S(Cys) $\pi \rightarrow Cu^{2+}$ $3d_{x^2-y^2}$ CT transitions, respectively). The lack of temperature dependence is different from the behavior of the T1 site in the Am loop mutant (*vide supra*) and in NiR (*vide infra*).

Variable temperature rR (77 and 295 K) spectra are shown in Fig. 16. The vibrational data show little variation upon warming; only a slight broadening is observed. The consistency of frequencies and the rR intensity distribution pattern ($\langle\nu$Cu-S(Cys)$\rangle = 396\ cm^{-1}$) indicate that there is a single species present at LT and room temperature (RT) with a Cu^{2+}–S(Cys) bond strength midway between that of Pc ($\langle\nu$Cu–S(Cys)$\rangle = 403\ cm^{-1}$) and of the green site in NiR ($\langle\nu$Cu–S(Cys)$\rangle = 388\ cm^{-1}$).

These results show that the spectral changes observed across the series of T1 sites in Fig. 12 do not result from variable amounts of two species in a mixture. Instead, the spectra reflect an individual species for each BC protein, which varies in geometric and electronic structure with the same ligand set (i.e. the coupled distortion). This demonstrates that the surrounding protein matrix can tune the geometric and electronic structure of the T1 site and thus affect function.

3.2. Temperature dependent perturbed Type 1 Cu sites

The absorption spectrum of NiR is similar to Paz in that it contains two moderately intense CT bands at low (~570 nm) and high (~460 nm) energy (Fig. 17) [70,75,76]. rR experiments on NiR have generated conflicting notions concerning the origin of the two absorption bands (i.e. one or multiple Cu species) [77,78]. In contrast to the above results on Paz, green NiR shows a remarkable set

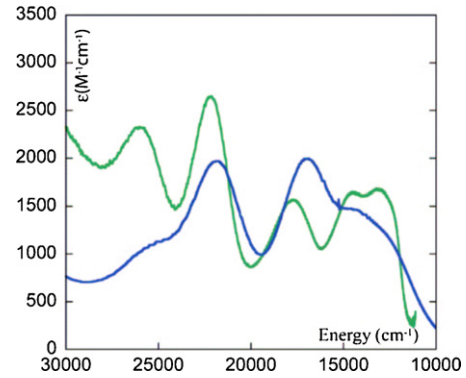

Fig. 17. Absorption spectra of resting WT NiR at 7K (green) and RT (blue). Reproduced from Ref. [22], © 2009 Proceedings of the National Academy of Sciences.

of temperature dependent spectral changes [22,70]. The LT absorption spectrum of NiR is shown in Fig. 17 (green line).

LT rR spectra of NiR using laser excitation at 458 and 568 nm are shown in Fig. 18A and B, respectively (solid green lines). Similar to Paz, at LT (77 K), the rR spectra of NiR show identical vibrational frequencies (364, 376, and 403 cm^{-1}), but very different intensity distribution patterns for 458 (σ) and 568 (π) nm excitation. This rR behavior is consistent with the presence of a single T1 Cu species at LT, exhibiting different excited state distortions for the ~460 and ~570 nm CT transitions. This LT species has a $\langle\nu$Cu-S(Cys)$\rangle$ of ~388 cm^{-1} (intensity weighted average using 568 nm excitation), reflecting a weaker Cu^{2+}–S(Cys) bond than either Pc (403 cm^{-1}) or other perturbed Cu sites such as Paz and CBP (396 and 394 cm^{-1}, respectively).

Large spectral changes occur upon increasing the temperature. The RT absorption spectrum is also shown in Fig. 17 (blue line). An intensity redistribution (i.e. higher intensity π and lower intensity σ CT) occurs along with a shift in the position of the CT energy maxima.

Upon going to RT, the rR spectra exhibit a reduction in overall intensity using 458 nm excitation (Fig. 18A) consistent with the reduced extinction coefficient of this band at RT. However, for 568 nm excitation at RT (Fig. 18B), a spectral change is observed. At LT the dominant feature is centered at 403 cm^{-1}, and, at RT, it shifts to 408 cm^{-1} with a moderately intense shoulder at 420 cm^{-1}. This increase in intensity weighted average from 388 to 407 cm^{-1} indicates a much stronger Cu^{2+}–S(Cys) bond at RT. These higher energy vibrational features are not present at LT, but grow in with increasing temperature, which indicates that there is a second T1 Cu species present at RT with a stronger Cu^{2+}–S(Cys) bond. The rR spectrum of the RT T1 Cu species can be obtained by subtracting the LT (77 K) rR spectrum of the pure green species from the RT data. The resultant spectrum (upon renormalization) is shown in the inset of Fig. 18B (blue line). It overlays very well with the rR data on the M182T variant of NiR (red line) [65]. This variant has no axial Met ligand [63,65]. Furthermore, the 364 cm^{-1} feature profiles the ~460 nm CT transition, while the 420 cm^{-1} feature profiles the ~600 nm CT transition (Fig. 18C).

The LT green site has a $\langle\nu$Cu–S(Cys)$\rangle$ of ~388 cm^{-1} while the pure high temperature form has a $\langle\nu$Cu–S(Cys)$\rangle$ of ~407 cm^{-1}, very similar to the M182T mutant ($\langle\nu$Cu-S(Cys)$\rangle$ of ~408 cm^{-1}). These data show that in NiR there are two distinct chromophores present at RT; one blue and one green T1 site with different Cu^{2+}-S(Cys) bond strengths reflecting a variation in the Cu^{2+}–S(Met) donor interaction. Only one chromophore is present at LT (i.e. a green Cu site).

The issue is, then, whether this is a thermodynamic equilibrium or a Boltzmann population of two electronic minima. Using the absorption spectrum of a pure green site (7 K, Fig. 17, green) and

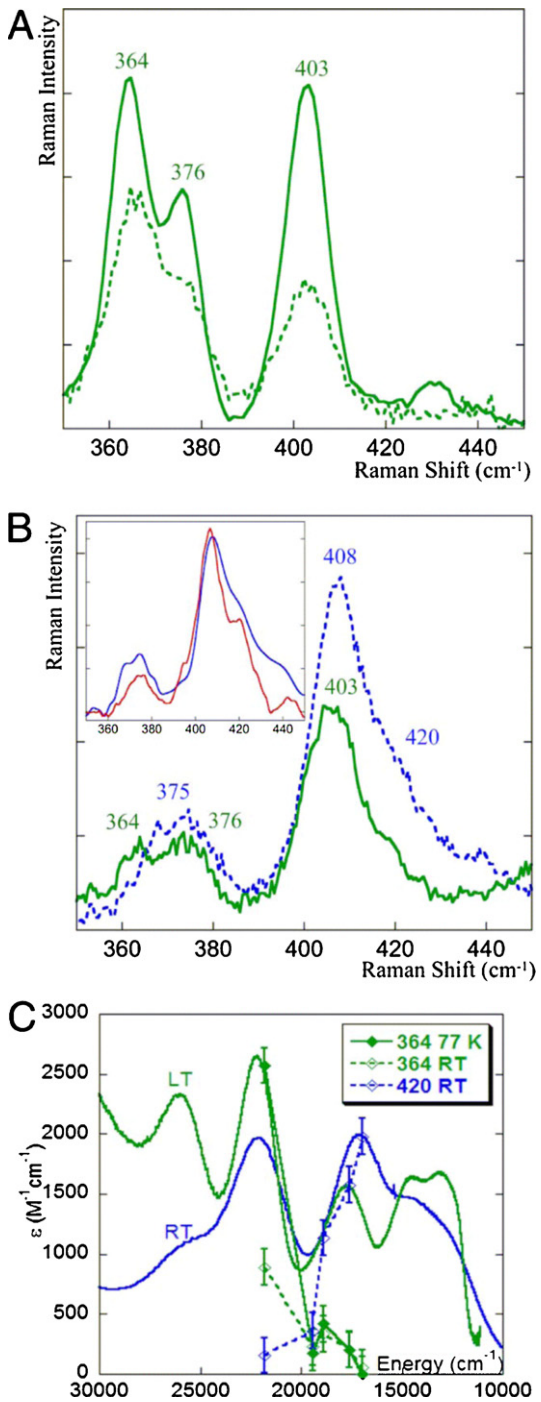

Fig. 18. Resonance Raman spectra of resting WT NiR with laser excitation at 458 nm (A) and 568 nm (B). 77 K spectra are in bold and RT spectra are in dotted lines. (Inset) Resonance Raman spectrum of the pure blue component of NiR (blue spectrum) and the M182T variant of NiR (red spectrum). (C) Resonance Raman profiles overlaid with the absorption spectra.
Reproduced from Ref. [22], © 2009 Proceedings of the National Academy of Sciences.

that of the previously studied M182T variant of NiR, temperature dependent absorption data of NiR were used to determine the relative amounts of the blue and green species. At 328 K there are 65% blue copper sites and 35% green copper sites. A Boltzmann population of two electronic minima would lead to a maximum 50/50 mixture. Therefore, the green and blue sites are in a thermodynamic equilibrium:

$$\text{Green} \overset{K_{eq}}{\longleftrightarrow} \text{Blue} \quad (8)$$

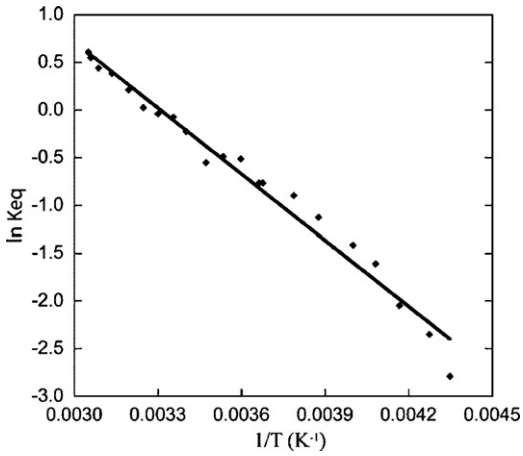

Fig. 19. Plot of $\ln K_{eq}$ vs. $1/T$, where $K_{eq} \approx 1$ at 298 K.
Reproduced from Ref. [22], © 2009 Proceedings of the National Academy of Sciences.

governed by an equilibrium constant, K_{eq}, which was obtained for the green to blue conversion at various temperatures. Plotting $\ln K_{eq}$ as a function of $1/T$ (Fig. 19) gives $\Delta H \approx 4.6$ kcal mol^{-1} from the slope and a $\Delta S \approx 15$ cal mol^{-1} K^{-1} ($T\Delta S \approx 4.5$ kcal mol^{-1} at 298 K) from the intercept. These thermodynamic parameters indicate that the green T1 Cu site is *enthalpically favored*, the only species present at LT; the blue form is *entropically favored*, its fraction increasing with temperature.

DFT calculations provide insight into these results. Full geometry optimization of a small model of the T1 site (no protein constraints) $[(Cu(im)_2(SCH_3)(S(CH_3)_2)]^+$ results in a structure very similar to that obtained for the green site in NiR from X-ray crystallography with a tetragonally distorted structure (more square planar) and Cu^{2+}–S(Cys) and Cu^{2+}–S(Met) bond distances of 2.18 and 2.41 Å, respectively. Removal of the thioether ligand results in a geometry optimized structure of the T1 site similar to the fungal laccases and Fet3p, and thus these two unconstrained optimizations with and without a thioether ligand represent the two extremes of the coupled distortion model. The thermodynamic properties of these sites were calculated using these models.

For the fully optimized models, the calculated dissociation energy for loss of the Cu^{2+}–S(Met) bond is 6.8 kcal mol^{-1} (solvated energy). The calculated entropy change is 39 cal mol^{-1} K^{-1}, which results in a $T\Delta S$ of 11.7 kcal mol^{-1} at 298 K (no solvated energy correction). The calculated change in enthalpy, ΔH, is consistent with the experimental results while the calculated $T\Delta S$ at 298 K is approximately 2.5 times too large. The low ΔH reflects a very weak Cu^{2+}–S(Met) bond as its loss is compensated by an increased strength of the Cu^{2+}–S(Cys) bond. The high calculated $T\Delta S$ reflects the fact that in NiR the thioether ligand is covalently linked to the protein backbone and is thus not fully lost upon going to RT.

3.3. The 'entatic' or 'rack-induced' state in plastocyanin

Potential energy surfaces (PESs) for Met binding further the understanding of the Met's influence on function. Fig. 20 shows the calculated PESs for Met binding in both the oxidized and reduced states. Pc has a Cu–S(Met) bond distance of 2.8–2.9 Å in the oxidized site. Geometry optimizing models with this bond distance constraint results in geometric structures very similar to crystallographic results on Pc, and the calculated ΔH and $T\Delta S$ of this model are similar to the 2.4 Å green model. Therefore, if Pc had an unconstrained Cu^{2+}–S(Met) bond it would exhibit similar temperature dependent spectral features as observed for green NiR. However, as for Paz and most other T1 sites, this is not the case. Thus the protein environment in these latter sites provides the constraints

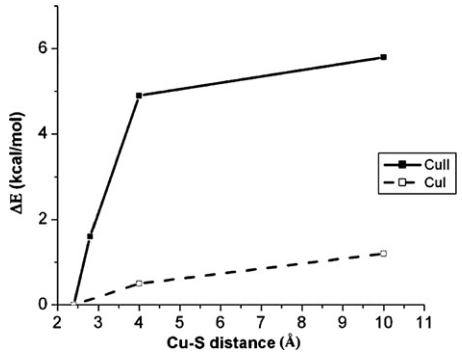

Fig. 20. Potential energy surfaces calculated as a function of Cu–S(thioether) distance for both cuprous (dashed line) and cupric (solid line) states (solvation included using a PCM with $\varepsilon = 4.0$).
Reproduced from Ref. [22], © 2009 Proceedings of the National Academy of Sciences.

necessary to oppose the entropy increase and prohibit Cu–S(Met) bond dissociation at physiological temperatures (Fig. 21). *This is the 'entatic' or 'rack-induced' state in BC proteins*.

One can further understand the contribution of this to function from the PES of the reduced site in Fig. 20. The Cu^+–S(Met) ΔH is calculated to be ~1 kcal/mol. This ΔH is much lower than that of the oxidized site, and thus constraining the S(Met) ligand stabilizes the oxidized more than the reduced state, lowering E^0 by ~200 mV.

In summary, from the above results, the temperature dependence of the spectral features of T1 Cu sites, as well as other metalloproteins with weak axial ligand coordination, can be used to determine whether or not the protein restricts ligand dissociation from the metal. The nature of the 'entatic' or 'rack-induced' state of the protein is that it does not allow this to occur in the majority of BC sites like Pc and Az. The temperature dependent spectral changes of NiR allowed us to experimentally determine the Cu^{2+}–S(Met) bond strength to be ~4.6 kcal/mol. This is a weak bond (due to its compensation by the S(Cys)) and this ligand should dissociate at elevated temperature. However, protein constraints overcome this entropic driving force, keeping the S(Met) ligand bound at physiological temperatures, tuning E^0 into the proper range for function.

4. Concluding comments

The study of BC proteins has been an evolutionary process. Above we have highlighted recent advances in understanding BC proteins; however, there are still important issues. The conserved ligand set, S(Cys), S(Met), and 2 N(His), gives rise to spectral features and properties due to protein constraints which derive from first coordination sphere effects. However, the contributions to function from the second coordination sphere are less well defined and less understood. From Table 1, with the same ligand set, the BC reduction potential can vary by >400 mV in different proteins. Recent work by Prof. Y. Lu has shown that, using only second sphere interactions, the E^0 of Az can be tuned over an even larger range

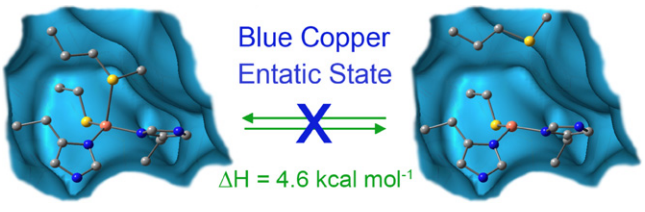

Fig. 21. Graphical representation of the 'entatic' or 'rack-induced' state in T1 BC proteins.

Table 1
Dependence of E^0 for different blue Cu proteins with the same ligand sets.

	Axial ligand and E^0 (mV)			Ref
	Phe/Leu/Thr	Met	Gln	
Fungal laccase	+770	+680		[80,102,103]
Azurin	+412	+310	+285	[104,105]
Cuc. stellacyanin	+500	+420	+260	[106,107]
Nitrite reductase	+354	+247		[63]
Rusticyanin	+800	+667	+563	[108]
Mavicyanin		+400	+213	[109]
Amicyanin		+250	+163	[110]

[79], and the nature of second sphere interactions in BC proteins (i.e. electrostatics, H-bonds, etc.) have yet to be fully and quantitatively defined. *Trametes versicolor* laccase and Fet3p have reduction potentials of ~790 [80] and ~430 mV [81], respectively, a difference of ~360 mV. X-ray crystal structures [82,83] have determined that both T1 sites contain a S(Cys), 2 N(His), structurally congruent ligand set. It is important to understand how such a difference exists when there is little variation in the second coordination sphere, and the role of solvent in this difference has yet to be defined.

BC proteins are often located in enzymes that carry out catalysis such as the four electron reduction of O_2 to H_2O in the multicopper oxidases (MCOs) [84,85] and the one electron reduction of nitrite to nitric oxide [86,87] in NiR. In both the MCOs and NiR, electrons from substrate are delivered to the catalytic site via the BC center. The high anisotropic covalency of the Cu^{2+}–S(Cys) bond couples the site into specific ET pathways. The S(Cys) is flanked in the sequence by His residues that are ligands to the remote Type 2 (NiR) and binuclear Type 3 (MCOs) Cu center. For both classes of enzymes there are two ET pathways. One is the Cys–His pathway, and the other is a pathway through an H-bond to the Cys carbonyl from the His ligand of the remote Cu (i.e. the H-bond shunt). The contribution of the latter can be affected by the redox state of the remote Cu site [45], and the presence of two pathways allows for the possibility of constructive or destructive interference [88]. The functional relevance of these two pathways and their potential interaction have yet to be defined.

As presented above, the 'entatic' or 'rack-induced' state in BC proteins is associated with protein constraints on a weak S(Met) ligand. Axial ligation by a S(Met) residue is also present in other active sites whose primary function is ET. These sites include Cu_A [89] and cytochrome c [90]. The strength of these metal–thioether bonds may also play important roles in ET, and the studies reviewed here in Section 3 provide the foundation for determining whether these involve protein constraints to affect reactivity (i.e. the 'entatic' or 'rack-induced' state).

For ET sites, Marcus theory [91–93] requires little change in geometry with oxidation. Thus, the concept of an 'entatic' or 'rack-induced' state is particularly appropriate. However, it can also play a role in biological function where large structural changes are required; for example, in cooperative O_2 binding. In the binuclear Cu site in hemocyanin, it appears that even though there is no bridging ligand in the deoxy state [94] the Cu's are kept in close proximity by the protein. In the relaxed quaternary geometry, the Cu^+–Cu^+ distance is ~3.6 Å [95–97] and there is significant electrostatic repulsion which destabilizes the reduced site and drives O_2 binding. In the tense quaternary structure the Cu^+–Cu^+ distance elongates to ~4.6 Å [94] reducing the electrostatic repulsion and stabilizing the reduced site [98,99].

In the field of bioinorganic chemistry, pioneered by Harry B. Gray, the protein is an ultimate ligand capable of playing many roles in controlling reactivity. The BC sites clearly demonstrate a number of these roles in ET function.

Acknowledgements

This work was supported by NSF CHE-0948211 (E.I.S.). SSRL operations are funded by the Department of Energy, Office of Basic Energy Sciences. The SSRL Structural Molecular Biology program is supported by the National Institutes of Health, National Center for Research Resources, Biomedical Technology Program, and the Department of Energy, Office of Biological and Environmental Research. R.G.H. is a Gerhard Casper Stanford Graduate Fellow. We gratefully acknowledge the major contributions of our co-workers and collaborators, who are cited in the referenced publications.

References

[1] R. Malkin, B.G. Malmstrom, Adv. Enzymol. Relat. Areas Mol. Biol. 33 (1970) 177–244.
[2] H.B. Gray, Chem. Soc. Rev. 15 (1986) 17–30.
[3] E.T. Adman, Adv Protein Chem, Academic Press, 1991, pp. 145–197.
[4] R.H. Holm, P. Kennepohl, E.I. Solomon, Chem. Rev. 96 (1996) 2239–2314.
[5] E.I. Solomon, R.K. Szilagyi, S. DeBeer George, L. Basumallick, Chem. Rev. 104 (2004) 419–458.
[6] B.L. Vallee, R.J. Williams, Proc. Natl. Acad. Sci. U.S.A. 59 (1968) 498–505.
[7] R.J.P. Williams, Eur. J. Biochem. 234 (1995) 363–381.
[8] B.G. Malmström, Eur. J. Biochem. 223 (1994) 711–718.
[9] E.I. Solomon, J.W. Hare, H.B. Gray, Proc. Natl. Acad. Sci. U.S.A. 73 (1976) 1389–1393.
[10] E.I. Solomon, P.J. Clendening, H.B. Gray, F.J. Grunthaner, J. Am. Chem. Soc. 97 (1975) 3878–3879.
[11] J. Mitchell Guss, H.C. Freeman, J. Mol. Biol. 169 (1983) 521–563.
[12] J.M. Guss, H.D. Bartunik, H.C. Freeman, Acta Crystallogr. Sect. B: Struct. Sci. B48 (1992) 790.
[13] K.W. Penfield, A.A. Gewirth, E.I. Solomon, J. Am. Chem. Soc. 107 (1985) 4519–4529.
[14] H.B. Gray, B.G. Malmström, R.J.P. Williams, J. Biol. Inorg. Chem. 5 (2000) 551–559.
[15] E.I. Solomon, K.W. Penfield, A.A. Gewirth, M.D. Lowery, S.E. Shadle, J.A. Guckert, L.B. LaCroix, Inorg. Chim. Acta 243 (1996) 67–78.
[16] S.M. Berry, M.D. Gieselman, M.J. Nilges, d.D.W.A. Van, Y. Lu, J. Am. Chem. Soc. 124 (2002) 2084–2085.
[17] S.M. Berry, M. Ralle, D.W. Low, N.J. Blackburn, Y. Lu, J. Am. Chem. Soc. 125 (2003) 8760–8768.
[18] R. Sarangi, S.I. Gorelsky, L. Basumallick, H.J. Hwang, R.C. Pratt, T.D.P. Stack, Y. Lu, K.O. Hodgson, B. Hedman, E.I. Solomon, J. Am. Chem. Soc. 130 (2008) 3866–3877.
[19] N. Kitajima, K. Fujisawa, M. Tanaka, Y. Morooka, J. Am. Chem. Soc. 114 (1992) 9232–9233.
[20] Y. Matsunaga, K. Fujisawa, N. Ibi, Y. Miyashita, K.-i. Okamoto, Inorg. Chem. 44 (2005) 325–335.
[21] S.I. Gorelsky, L. Basumallick, J. Vura-Weis, R. Sarangi, K.O. Hodgson, B. Hedman, K. Fujisawa, E.I. Solomon, Inorg. Chem. 44 (2005) 4947–4960.
[22] S. Ghosh, X. Xie, A. Dey, Y. Sun, C.P. Scholes, E.I. Solomon, Proc. Natl. Acad. Sci. U.S.A. 106 (2009) 4969–4974.
[23] T. Glaser, B. Hedman, K.O. Hodgson, E.I. Solomon, Acc. Chem. Res. 33 (2000) 859–868.
[24] S.E. Shadle, J.E. Penner-Hahn, H.J. Schugar, B. Hedman, K.O. Hodgson, E.I. Solomon, J. Am. Chem. Soc. 115 (1993) 767–776.
[25] R.C. Pratt, L.M. Mirica, T.D.P. Stack, Inorg. Chem. 43 (2004) 8030–8039.
[26] A.A. Gewirth, E.I. Solomon, J. Am. Chem. Soc. 110 (1988) 3811–3819.
[27] K.W. Penfield, R.R. Gay, R.S. Himmelwright, N.C. Eickman, V.A. Norris, H.C. Freeman, E.I. Solomon, J. Am. Chem. Soc. 103 (1981) 4382–4388.
[28] B.S. Gerstman, A.S. Brill, J. Chem. Phys. 82 (1985) 1212–1230.
[29] F. Neese, E.I. Solomon, Inorg. Chem. 38 (1999) 1847–1865.
[30] J. Yoon, L.M. Mirica, T.D.P. Stack, E.I. Solomon, J. Am. Chem. Soc. 127 (2005) 13680–13693.
[31] O. Siiman, N.M. Young, P.R. Carey, J. Am. Chem. Soc. 96 (1974) 5583–5585.
[32] V. Miskowski, S.P.W. Tang, T.G. Spiro, E. Shapiro, T.H. Moss, Biochemistry 14 (1975) 1244–1250.
[33] O. Siiman, N.M. Young, P.R. Carey, J. Am. Chem. Soc. 98 (1976) 744–748.
[34] N.S. Ferris, W.H. Woodruff, D.L. Tennent, D.R. McMillin, Biochem. Biophys. Res. Commun. 88 (1979) 288–296.
[35] T.J. Thamann, P. Frank, L.J. Willis, T.M. Loehr, Proc. Natl. Acad. Sci. U.S.A. 79 (1982) 6396–6400.
[36] D.F. Blair, G.W. Campbell, V. Lum, C.T. Martin, H.B. Gray, B.G. Malmstroem, S.I. Chan, J. Inorg. Biochem. 19 (1983) 65–73.
[37] W.H. Woodruff, K. Norton, B.I. Swanson, H.A. Fry, B.G. Malmström, I. Pecht, D.F. Blair, W. Cho, G.W. Campbell, V. Lum, V.M. Miskowski, S.I. Chan, H.B. Gray, Inorg. Chim. Acta 79 (1983) 51–52.
[38] W.H. Woodruff, K.A. Norton, B.I. Swanson, H.A. Fry, J. Am. Chem. Soc. 105 (1983) 657–658.
[39] L. Nestor, J.A. Larrabee, G. Woolery, B. Reinhammar, T.G. Spiro, Biochemistry 23 (1984) 1084–1093.
[40] W.H. Woodruff, K.A. Norton, B.I. Swanson, H.A. Fry, Proc. Natl. Acad. Sci. U.S.A. 81 (1984) 1263–1267.
[41] D.F. Blair, G.W. Campbell, W.K. Cho, A.M. English, H.A. Fry, V. Lum, K.A. Norton, J.R. Schoonover, S.I. Chan, J. Am. Chem. Soc. 107 (1985) 5755–5766.
[42] J. Han, E.T. Adman, T. Beppu, R. Codd, H.C. Freeman, L. Huq, T.M. Loehr, J. Sanders-Loehr, Biochemistry 30 (1991) 10904–10913.
[43] S. Dong, T.G. Spiro, J. Am. Chem. Soc. 120 (1998) 10434–10440.
[44] D. Qiu, S. Dasgupta, P.M. Kozlowski, W.A. Goddard, T.G. Spiro, J. Am. Chem. Soc. 120 (1998) 12791–12797.
[45] A.J. Augustine, M.E. Kragh, R. Sarangi, S. Fujii, B.D. Liboiron, C.S. Stoj, D.J. Kosman, K.O. Hodgson, B. Hedman, E.I. Solomon, Biochemistry 47 (2008) 2036–2045.
[46] D.R. McMillin, R.C. Rosenberg, H.B. Gray, Proc. Natl. Acad. Sci. U.S.A. 71 (1974) 4760–4762.
[47] D.L. Tennent, D.R. McMillin, J. Am. Chem. Soc. 101 (1979) 2307–2311.
[48] B.A.J. Di, T.K. Chang, B.G. Malmstroem, H.B. Gray, B.G. Karlsson, M. Nordling, T. Pascher, L.G. Lundberg, Inorg. Chim. Acta 198–200 (1992) 145–148.
[49] H. Nar, R. Huber, A. Messerschmidt, A.C. Filippou, M. Barth, M. Jaquinod, d.K.M. Van, G.W. Canters, Eur. J. Biochem. 205 (1992) 1123–1129.
[50] J.M. Moratal, A. Romero, J. Salgado, A. Perales-Alarcon, H.R. Jimenez, Eur. J. Biochem. 228 (1995) 653–657.
[51] H.R. Jimenez, J. Salgado, J.M. Moratal, I. Morgenstern-Badarau, Inorg. Chem. 35 (1996) 2737–2741.
[52] N. Bonander, T. Vanngard, L.-C. Tsai, V. Langer, H. Nar, L. Sjoelin, Proteins: Struct. Funct. Genet. 27 (1997) 385–394.
[53] Z.-W. Chen, M.J. Barber, W.S. McIntire, F.S. Mathews, Acta Crystallogr. Sect. D: Biol. Crystallogr. D54 (1998) 253–268.
[54] K.J.O.A. De, K. Pierloot, U. Ryde, J. Phys. Chem. B 103 (1999) 8375–8382.
[55] T. Funk, P. Kennepohl, B.A.J. Di, W.A. Wehbi, A.T. Young, S. Friedrich, E. Arenholz, H.B. Gray, S.P. Cramer, J. Am. Chem. Soc. 126 (2004) 5859–5866.
[56] I. Mayer, Chem. Phys. Lett. 97 (1983) 270–274.
[57] I. Mayer, Theor. Chim. Acta 67 (1985) 315–322.
[58] I. Mayer, Int. J. Quantum Chem. 29 (1986) 477–483.
[59] I. Mayer, Int. J. Quantum Chem. 29 (1986) 73–84.
[60] H. Irving, R.J.P. Williams, Nature (London, UK) 162 (1948) 746–747.
[61] H. Irving, R.J.P. Williams, J. Chem. Soc. (1953) 3192.
[62] H. Irving, R.J.P. Williams, Nature (1954) 746.
[63] K. Olesen, A. Veselov, Y. Zhao, Y. Wang, B. Danner, C.P. Scholes, J.P. Shapleigh, Biochemistry 37 (1998) 6086–6094.
[64] A. Veselov, K. Olesen, A. Sienkiewicz, J.P. Shapleigh, C.P. Scholes, Biochemistry 37 (1998) 6095–6105.
[65] L. Basumallick, R.K. Szilagyi, Y. Zhao, J.P. Shapleigh, C.P. Scholes, E.I. Solomon, J. Am. Chem. Soc. 125 (2003) 14784–14792.
[66] J.M. Guss, P.R. Harrowell, M. Murata, V.A. Norris, H.C. Freeman, J. Mol. Biol. 192 (1986) 361–387.
[67] J.A. Guckert, M.D. Lowery, E.I. Solomon, J. Am. Chem. Soc. 117 (1995) 2817–2844.
[68] E.I. Solomon, D.W. Randall, T. Glaser, Coord. Chem. Rev. 200–202 (2000) 595–632.
[69] L.B. LaCroix, D.W. Randall, A.M. Nersissian, C.W.G. Hoitink, G.W. Canters, J.S. Valentine, E.I. Solomon, J. Am. Chem. Soc. 120 (1998) 9621–9631.
[70] L.B. LaCroix, S.E. Shadle, Y. Wang, B.A. Averill, B. Hedman, K.O. Hodgson, E.I. Solomon, J. Am. Chem. Soc. 118 (1996) 7755–7768.
[71] K. Pierloot, J.O.A. De Kerpel, U. Ryde, M.H.M. Olsson, B.r.O. Roos, J. Am. Chem. Soc. 120 (1998) 13156–13166.
[72] P. Comba, V. Mueller, R. Remenyi, J. Inorg. Biochem. 98 (2004) 896–902.
[73] S.R. Pauleta, F.o. Guerlesquin, C.F. Goodhew, B. Devreese, J. Van Beeumen, A.S. Pereira, I. Moura, G.W. Pettigrew, Biochemistry 43 (2004) 11214–11225.
[74] X. Xie, R.G. Hadt, S.R. Pauleta, P.J. González, S. Un, I. Moura, E.I. Solomon, J. Inorg. Biochem. 103 (2009) 1307–1313.
[75] H. Iwasaki, S. Noji, S. Shidara, J. Biochem. 78 (1975) 355–361.
[76] M.Y. Liu, M.C. Liu, W.J. Payne, J. Legall, J. Bacteriol. 166 (1986) 604–608.
[77] D.M. Dooley, R.S. Moog, M.Y. Liu, W.J. Payne, J. LeGall, J. Biol. Chem. 263 (1988) 14625–14628.
[78] J. Han, T.M. Loehr, Y. Lu, J.S. Valentine, B.A. Averill, J. Sanders-Loehr, J. Am. Chem. Soc. 115 (1993) 4256–4263.
[79] N.M. Marshall, D.K. Garner, T.D. Wilson, Y.-G. Gao, H. Robinson, M.J. Nilges, Y. Lu, Nature (London, UK) 462 (2009) 113–116.
[80] F. Xu, A.E. Palmer, D.S. Yaver, R.M. Berka, G.A. Gambetta, S.H. Brown, E.I. Solomon, J. Biol. Chem. 274 (1999) 12372–12375.
[81] T.E. Machonkin, L. Quintanar, A.E. Palmer, R. Hassett, S. Severance, D.J. Kosman, E.I. Solomon, J. Am. Chem. Soc. 123 (2001) 5507–5517.
[82] K. Piontek, M. Antorini, T. Choinowski, J. Biol. Chem. 277 (2002) 37663–37669.
[83] A.B. Taylor, C.S. Stoj, L. Ziegler, D.J. Kosman, P.J. Hart, Proc. Natl. Acad. Sci. U.S.A. 102 (2005) 15459–15464.
[84] A. Messerschmidt, R. Ladenstein, R. Huber, M. Bolognesi, L. Avigliano, R. Petruzzelli, A. Rossi, A. Finazzi-Agró, J. Mol. Biol. 224 (1992) 179–205.
[85] E.I. Solomon, A.J. Augustine, J. Yoon, Dalton Trans. (2008) 3921–3932.
[86] C.L. Hulse, J.M. Tiedje, B.A. Averill, Anal. Biochem. 172 (1988) 420–426.
[87] J.W. Godden, S. Turley, D.C. Teller, E.T. Adman, M.Y. Liu, W.J. Payne, J. LeGall, Science (Washington, DC, 1883–) 253 (1991) 438–442.
[88] I.A. Balabin, J. Onuchic, Science 290 (2000) 114–117.
[89] H. Robinson, M.C. Ang, Y.-G. Gao, M.T. Hay, Y. Lu, A.H.J. Wang, Biochemistry 38 (1999) 5677–5683.

[90] R.E. Dickerson, T. Takano, D. Eisenberg, O.B. Kallai, L. Samson, A. Cooper, E. Margoliash, J. Biol. Chem. 246 (1971) 1511–1535.
[91] R.A. Marcus, N. Sutin, Biochim. Biophys. Acta Rev. Bioenerg. 811 (1985) 265–322.
[92] D.N. Beratan, J.N. Betts, J.N. Onuchic, Science (Washington, DC, 1883–) 252 (1991) 1285–1288.
[93] M.D. Newton, Chem. Rev. 91 (1991) 767–792.
[94] B. Hazes, K.H. Kalk, W.G. Hol, K.A. Magnus, C. Bonaventura, J. Bonaventura, Z. Dauter, Protein Sci. 2 (1993) 597–619.
[95] W.P.J. Gaykema, W.G.J. Hol, J.M. Vereijken, N.M. Soeter, H.J. Bak, J.J. Beintema, Nature (Lond.) 309 (1984) 23–29.
[96] W.P.J. Gaykema, A. Volbeda, W.G.J. Hol, J. Mol. Biol. 187 (1986) 255–275.
[97] A. Volbeda, W.G.J. Hol, J. Mol. Biol. 209 (1989) 249–279.
[98] M. Metz, E.I. Solomon, J. Am. Chem. Soc. 123 (2001) 4938–4950.
[99] J. Yoon, S. Fujii, E.I. Solomon, Proc. Natl. Acad. Sci. U.S.A. 106 (2009) 6585–6590.
[100] E.I. Solomon, Inorg. Chem. 45 (2006) 8012–8025.
[101] L. Basumallick, R. Sarangi, G.S. DeBeer, B. Elmore, A.B. Hooper, B. Hedman, K.O. Hodgson, E.I. Solomon, J. Am. Chem. Soc. 127 (2005) 3531–3544.
[102] D.S. Yaver, F. Xu, E.J. Golightly, K.M. Brown, S.H. Brown, M.W. Rey, P. Schneider, T. Halkier, K. Mondorf, H. Dalboge, Appl. Environ. Microbiol. 62 (1996) 834–841.
[103] F. Xu, R.M. Berka, J.A. Wahleithner, B.A. Nelson, J.R. Shuster, S.H. Brown, A.E. Palmer, E.I. Solomon, Biochem. J. 334 (1998) 63–70.
[104] T. Pascher, B.G. Karlsson, M. Nordling, B.G. Malmstrom, T. Vanngard, Eur. J. Biochem. 212 (1993) 289–296.
[105] A. Romero, C.W.G. Hoitink, H. Nar, R. Huber, A. Messerschmidt, G.W. Canters, J. Mol. Biol. 229 (1993) 1007–1021.
[106] A.M. Nersissian, M.G. Hill, J.S. Valentine, Personal Communication, 2003.
[107] A.M. Nersissian, C. Immoos, M.G. Hill, P.J. Hart, G. Williams, R.G. Herrmann, J.S. Valentine, Protein Sci. 7 (1998) 1915–1929.
[108] J.F. Hall, L.D. Kanbi, R.W. Strange, S.S. Hasnain, Biochemistry 38 (1999) 12675–12680.
[109] K. Kataoka, M. Nakai, K. Yamaguchi, S. Suzuki, Biochem. Biophys. Res. Commun. 250 (1998) 409–413.
[110] R.E.M. Diederix, G.W. Canters, C. Dennison, Biochemistry 39 (2000) 9551–9560.